THE UNIVERSITY of EDINBURGH

Edinburgh Research Explorer

Recent progress in SnO2/g-C3N4 heterojunction photocatalysts: Synthesis, modification, and application

Citation for published version:
Ren, W, Yang, J, Zhang, J, Li, W, Sun, C, Zhao, H, Wen, Y, Sha, O & Liang, B 2022, 'Recent progress in SnO2/g-C3N4 heterojunction photocatalysts: Synthesis, modification, and application', *Journal of alloys and compounds*, vol. 906, pp. 164372. https://doi.org/10.1016/j.jallcom.2022.164372

Digital Object Identifier (DOI):
10.1016/j.jallcom.2022.164372

Link:
Link to publication record in Edinburgh Research Explorer

Document Version:
Peer reviewed version

Published In:
Journal of alloys and compounds

General rights
Copyright for the publications made accessible via the Edinburgh Research Explorer is retained by the author(s) and / or other copyright owners and it is a condition of accessing these publications that users recognise and abide by the legal requirements associated with these rights.

Take down policy
The University of Edinburgh has made every reasonable effort to ensure that Edinburgh Research Explorer content complies with UK legislation. If you believe that the public display of this file breaches copyright please contact openaccess@ed.ac.uk providing details, and we will remove access to the work immediately and investigate your claim.

OPEN ACCESS

Download date: 25. Nov. 2022

Recent Progress in SnO_2/g-C_3N_4 Heterojunction Photocatalysts: Synthesis, Modification, and Application

Wangwei Ren[1], Jingkai Yang[1*], Jiaxin Zhang[1], Wei Li[2], Chaoyang Sun[1], Hongli Zhao[1], Yintang Wen[1], Ou Sha[1], Bo Liang[1*]

[1]State Key Laboratory of Metastable Materials Science and Technology, Key Laboratory of Applied Chemistry, Yanshan University, Qinhuangdao, 066004, China

[2]Institute for Materials and Processes, School of Engineering, University of Edinburgh, Mayfield Road, Edinburgh EH9 3JL, UK

Corresponding author: yangjk@ysu.edu.cn (Jingkai Yang), liangbo@ysu.edu.cn (Bo Liang)

Abstract: Semiconductor photocatalysts, especially semiconductor heterojunctions, have great development potential in the field of photocatalysis. SnO_2/g-C_3N_4 heterojunction has shown excellent photocatalytic performance rather than single SnO_2 or g-C_3N_4, particularly for visible-light-driven photocatalysis. In this review, the synthesis methods of SnO_2/g-C_3N_4 heterojunction are summarized. Then, the modification strategies of morphology control, defect introduction and multiple structural optimization strategies are highlighted. Morever, the possible mechanisms and applications in environment remediation and energy conversion of SnO_2/g-C_3N_4 heterojunction are discussed. Finally, the challenges and perspectives of SnO_2/g-C_3N_4 heterojunction are also proposed.

Keywords: SnO_2/g-C_3N_4 photocatalysts; heterojunction; synthesis; modification; application

Contents

1. Introduction

Photocatalytic technology may provide a new way to solve some grand challenges such as environment remediation and energy conversion, which contribute to sustainability and resilience of the earth. Due to its environmental advantages, suitable photocatalyts can directly utilize sunlight to generate hydrogen [1, 2], degrade pollutants [3] and reduce CO_2 [4], etc. Therefore, it is worth pursuing to design a photocatalyst with high efficiency, visible light response activity, environmental friendliness and good stability. At present, the research of semiconductor photocatalysts has made some achievements, but there are still some problems to be solved urgently.

SnO_2 is an n-type wide band gap semiconductor with advantages of environmentally friendly, non-toxic, low-cost and excellent photoelectrochemical performance. In particular, its lower conduction band (CB) position is considered to be a better electron acceptor than TiO_2 and ZnO. However, the inherent disadvantage of SnO_2 is the wide band gap (Eg=3.6 eV), which can only absorb ultraviolet light (only 5% of the sunlight), resulting in low utilization of solar energy. In order to make use of the above advantages and achieve more excellent photocatalytic efficiency on SnO_2 based materials, many modification methods have been carried out. Among these modifications, to construct a heterojunction with relatively narrower bandgap semiconductor may be a promising way, such as SnO_2/CdS [5-7], SnO_2/ZnO [8-10], SnO_2/SnS_2 [11-13], SnO_2/$BiVO_4$ [14-16], SnO_2/Fe_2O_3 [17-19], etc. Nowadays, two-dimensional structure graphitized carbon nitride (g-C_3N_4, Eg=2.7 eV) has attracted more and more attention to couple with SnO_2, which is due to its suitable band structure, metal-free, simple preparation process, strong visible light absorption capacity, and good physical and chemical stability. However, the photocatalytic performance of g-C_3N_4 is limited by its high photogenerated carrier recombination.

In theory, the well-matched position of the conduction band and valence band (VB) of SnO_2 (E_{CB}=-0.07 eV, E_{VB}=3.53 eV, vs.NHE) and g-C_3N_4 (E_{CB}= -1.13 eV, E_{VB}=1.57 eV, vs.NHE) [20] can achieve the desired goal of good separation of photogenerated

charge carriers. In the band structure of rutile SnO_2, the O 2p state contributes to the top of VB, and the bottom of CB is mainly composed of Sn 5s, 5p and O 2p states [21, 22]. On the other hand, in the band structure of g-C_3N_4 (Eg=2.7 eV)[23, 24], the top of VB is occupied by σ bond that formed by sp2 hybridization of 2s, $2p_x$, $2p_y$ orbitals of C and N atoms, while the bottom of CB is constituted of π* anti-bond that formed by $2p_z$ orbit of C and N atoms. When g-C_3N_4 contacts with SnO_2, and the work function difference causes band bending at the contact interface. An internal electric field will be generated between the depletion layer and the accumulation layer, which is beneficial to prolong the lifetime of photogenerated charge carriers [25]. Therefore, coupling SnO_2 with g-C_3N_4 can be promising to construct an efficient visible-light-driven heterojunction to effectively separate photogenerated electrons and holes.

In summary, SnO_2/g-C_3N_4 heterojunction can exhibit good photocatalytic performance due to the synergistic effect of SnO_2 and g-C_3N_4. However, there are still some unsolved problems, such as the complex preparation steps, weak interface bonding and small contact area, as well as the gross aggregation and random loading of SnO_2 on g-C_3N_4, which are still obstacles to the large-scale applications of SnO_2/g-C_3N_4 photocatalyst. Therefore, it's necessary to review the present research achievements to provide a clear guide for the future development. In this work, the modification strategies of SnO_2/g-C_3N_4 heterojunction have been discussed in detail, including morphology control, defect introduction (heteroatom doping and vacancy introduction) and multiple structure optimization strategies (co-catalyst loading, ternary heterostructure). And the possible mechanisms and applications of SnO_2/g-C_3N_4 photocatalyst are summarized. Finally, the development prospects of SnO_2/g-C_3N_4 photocatalyst are provided.

2. Synthesis methods of SnO_2/g-C_3N_4 heterojunction

Mastering the physical properties of materials is very helpful for the selection of synthesis conditions and application environment. Here, the physical properties of SnO_2

and g-C_3N_4 are briefly summarized. SnO_2 is generally white powder with density (6.85 g/cm^3), melting point (1630℃) and stable performance at room temperature and pressure. It is insoluble in water, alcohol and strong acid, but soluble in sodium hydroxide and potassium hydroxide. And g-C_3N_4 is generally light yellow powder, which is a planar two-dimensional lamellar structure similar to graphene. It is an infinite network of basic structural units (triazine ring (C_3N_3) or heptazine ring (C_6N_7)), and the two-dimensional nanosheets are connected by van der Waals forces. Its density is about 0.114 g/cm^3. In addition, it has good thermal stability at high temperature (< 600℃) and stable performance in strong acid and alkali environment.

The difference of synthesis process (i.e. reaction conditions, raw materials, the proportion variation, etc.) can produce SnO_2/g-C_3N_4 photocatalysts with various photocatalytic performances. It is an interesting and attractive subject to explore the most suitable synthesis method to obtain optimized SnO_2/g-C_3N_4. Usually, the combination of SnO_2 and g-C_3N_4 or the synthesis of SnO_2/g-C_3N_4 heterojunction with a wider and tighter contact surface is favorable but challenging. Different synthesis routes can obtain distinct morphologies to regulate the heterojunction interface contact, including 0D-2D point-to-face contact, 1D-2D line-to-face contact, 2D-2D face-to-face contact, etc. Some synthesis methods of SnO_2/g-C_3N_4 heterojunction composites have been listed as follows: ultrasonic-assisting deposition method, hydrothermal/solvothermal method, solid-phase method, sol-gel method, in-situ co-pyrolysis method, and so on. From another perspective, the preparation process can start with SnO_2 + g-C_3N_4, SnO_2 precursor + g-C_3N_4, g-C_3N_4 precursor + SnO_2, or SnO_2 precursor + g-C_3N_4 precursor. The synthesis methods of SnO_2/g-C_3N_4 heterojunction are summarized in Table 1 and discussed in detail below.

2.1 Ultrasonic-assisting deposition method

The ultrasonic-assisting deposition method with simple equipment and easy operation, but it highly depends on the pre-prepared SnO_2 and g-C_3N_4 [26-28]. It can directly control the mass ratio of the SnO_2/g-C_3N_4 composite with different proportions. However, the obvious disadvantage is that the chemical reaction is too complicated to

control the component accurately. Usually, the pre-prepared g-C_3N_4 and SnO_2 are dispersed in water or organic solvents to form turbid suspensions, and then the binding force between them can be enhanced by ultrasonication and vigorous stirring to form SnO_2/g-C_3N_4 intimate contact interface. To confirm the success of heterostructure construction, Zang et al. [29] prepared mechanically mixed sample for comparison. In Fig. 1, the clear interface between SnO_2 and g-C_3N_4 of the composites synthesized by ultrasonic-assisting deposition method can be observed, which is completely different from that of the mechanically mixed sample. At the same time, the other stronger evidence is from XPS analysis results (Fig. 2) that the C 1s and N 1s signal peaks shift to higher binding energy and Sn 3d peak to lower binding energy [30-32]. Therefore, the redistribution of charge density of interface confirms the tight interaction of SnO_2/g-C_3N_4 heterojunction. It is elucidated that the ultrasonic-assisting deposition method can obtain heterojunction with close interface. The SnO_2/g-C_3N_4 heterojunction photocatalytic degradation efficiency of methyl orange (MO) is 73% in 180 min, which is much higher than that of mechanically mixed sample (20% in 180 min).

2.2 Hydrothermal/solvothemal method

The hydrothermal/solvothermal method is one of the most frequently used methods to prepare SnO_2/g-C_3N_4 heterojunction. It has obvious advantages such as simple fabrication process, no need for high-temperature calcination, and effectively avoiding crystal agglomeration. In addition, the reaction conditions (pH, temperature, time and other parameters) can be easily adjusted to obtain crystals of different morphologies and sizes. Compared with the ultrasonic-assisting deposition method, the synthesis step is simplified because it is not necessary to pre-prepare SnO_2 or g-C_3N_4. The well-crystallized SnO_2/g-C_3N_4 heterojunction can be obtained by the hydrothermal process of uniformly dispersed tin chloride and g-C_3N_4 solution in a highly airtight environment [33-35]. However, hydrothermal reaction vessel makes it difficult to monitor and adjust reaction conditions in real time, which is needed for optimized and controlled reactions.

Moreover, the spontaneous nucleation and growth of crystals during the natural

cooling process of the solution in the reactor are more difficult for manual intervention and sometimes the crystallization is incomplete. But this can be utilized to prepare highly efficient photocatalysts. Ji et al. [36] observed that the SnO_2 layered nanosheets in the prepared SnO_2/g-C_3N_4 composite showed irregular shapes and sizes, which are different from the ordinary SnO_2 nanosheets in the previous literature (thin and structured morphology)[32, 37]. This may be the incomplete crystallization of SnO_2 caused by the uneven cooling of the reactor. It is worth noting that the degradation efficiency of rhodamine b (RhB) by this special SnO_2/g-C_3N_4 under visible light (92% in 3h) is nearly 9 times and 2.5 times higher than that of original SnO_2 (10% in 3h) and g-C_3N_4 (36% in 3h), which is due to the visible light absorption of incomplete crystallization of SnO_2.

Remarkably enough, SnO_2/g-C_3N_4 prepared by hydrothermal or solvothermal method can be further processed to achieve enhanced heterojunction interface contact. For example, the ball milling treatment [33] can not only transform the bulk g-C_3N_4 into nanosheets, but also significantly reduce the agglomeration of SnO_2, which can obtain a large number of point-to-face contacts of SnO_2/g-C_3N_4 composite to promote charge transfer. Although the photoresponse of the ball-milled SnO_2/g-C_3N_4 is slightly blue-shifted due to the quantum size effect caused by some small grains with thin edges, this negative effect can be compensated by its superior carrier separation ability. In general, the ball milling treatment has a positive effect on the SnO_2/g-C_3N_4 photocatalytic activity.

2.3 Solid-phase method

The low-cost solid-phase method without expensive organic solvents can effectively avoid the risk of water pollution, which caused by the liquid-phase solvothermal method. In addition, this method possesses the advantages of high yield, convenient operation, and controllable reaction conditions [38-40]. However, it also has disadvantages such as poor uniformity of particle size distribution, agglomeration, and easy introduction of impurities. Fettkenhauer et al. [41] prepared the SnO_2/g-C_3N_4 heterojunction through the condensation reaction of dicyandiamide in different alkali

metal chloride salt melts ($MCl/SnCl_2$ (M=Li, Na, K, Cs)). The Sn-N Lewis acid-base bonds are formed by $SnCl_2$ and dicyandiamide in the solid-phase reaction, which could dissolve precursors and some intermediate products to promote the continuous progress of the solid-phase reaction. Moreover, g-C_3N_4 nanosheets with a specific surface area up to 220 $m^2 \cdot g^{-1}$ can be directly obtained by solid-phase method without additional exfoliation process (Fig. 3). The effects of different reaction conditions were also investigated, such as the type of salt melt, reaction temperature and the ratio of g-C_3N_4 precursor to salt melt, etc. The results show that SnO_2/g-C_3N_4 photocatalyst obtained under the conditions of $KCl/SnCl_2$ melt, synthesis temperature of 550 ℃ and the ratio of precursor to salt melt of 1:20 possess the highest degradation efficiency of RhB and stable hydrogen production. Thereafter, Shen et al. [20] obtained SnO_2@g-C_3N_4 with core-shell structure through solid-phase method by using SnO_2 microspheres and molten urea. This face-to-face core-shell structure undoubtedly increases the intimate contact area of heterojunction and promotes the efficiency of carrier transport and separation, and the RhB degradation efficiency of SnO_2@g-C_3N_4 is more than 75% in 120 min (Fig. 4).

2.4 Sol-gel method

The sol-gel method can synthesize photocatalysts with large specific surface area, high porosity or ultra-uniform distribution of multi-component molecules. In the whole process, the transformation of material state involves solution, sol, gel and crystal (or amorphous). Generally, the preparation process takes a longer average period at low temperatures (a few days or even weeks), and usually requires subsequent high-temperature calcination to remove possible impurities. Li et al. [42] used the sol-gel method to prepare g-C_3N_4/SiO_2/SnO_2 porous materials, and SiO_2 was derived from the introduction of tetraethyl orthosilicate (TEOS) to promote gel formation. In addition, the existence of SiO_2 may weakly prevent some electrons transfer and reduce the recombination of electrons and holes, but this requires additional evidence [43]. As a result, a gel blocky structure with slice layer assembled by gel particles was obtained (Fig. 5). The loose and porous structure can provide more reaction sites and promote

carrier separation, so the photocatalytic degradation efficiency of RhB reached 95.10% in 90 min under visible light.

2.5 In situ co-pyrolysis method

The in situ co-pyrolysis method has outstanding advantages of simplicity and convenience. In these above methods, SnO_2/g-C_3N_4 composite is synthesized based on a multi-step synthesis procedure which may require the use of pre-prepared SnO_2 or g-C_3N_4, resulting in the overall synthesis process becoming complicated. The in situ co-pyrolysis method can simultaneously decompose the precursors of SnO_2 and g-C_3N_4 in one step, which simplifies the heterogeneous bonding process to some extent. There is no doubt that the in situ growth process can obtain a tighter heterojunction interface, and the various gases released by the pyrolysis of precursors can reduce the agglomeration of nanoparticles. In recent study, three-dimensional porous structure was obtained by using $SnCl_4$ and thiourea [44]. And g-C_3N_4 network formed in the co-pyrolysis process is penetrated by a large number of bubbles which released by the decomposition of $SnCl_4$ (like HCl, SOx), which can minimize agglomeration (Fig. 6). From the perspective of environmental protection, Seza et al. [45] prepared SnO_2/g-C_3N_4 heterojunction by co-pyrolysis of tin source and urea under microwave-assisted conditions, in which tin was dissolved in HCl as tin source to simulate the similar situation of recovering tin from metal waste in the future. Microwave can provide a large amount of energy in a short period of time, leading to the rapid formation of SnO_2 nanoparticles, which are connected to each other through Sn-O-Sn bridges. Then, the intermediate product (isocyanic acid) of urea pyrolysis will form g-C_3N_4 with the help of the surface of existing nanoparticles. The result shows that some gaseous products (NH_3 and CO_2, etc.) of the complete pyrolysis of urea may collide with nanoparticles, which can significantly inhibit the growth and agglomeration of the particles. And during the co-pyrolysis of melamine and $Sn(OH)_4$, a large amount of gaseous products (such as NH_3) produced by the decomposition of melamine create an oxygen-poor environment, so that $Sn(OH)_4$ is reduced to SnO_2 nanoparticles with oxygen-rich vacancies [46] The oxygen-rich vacancy SnO_{2-x}/g-C_3N_4 exhibited excellent

photocatalytic activity for RhB, and the degradation rate constant is 0.0226 min^{-1}, which is 32.28 and 5.79 times higher than that of SnO_2 and g-C_3N_4, respectively.

Regardless of the synthesis method used to prepare SnO_2/g-C_3N_4 heterojunction composites, it is hoped to reduce agglomeration as much as possible. In addition, it is reported that the freeze-drying technique can be used to quickly sublime water at low temperature (about -20°C) to dry the sample [47], which is different from the traditional evaporative drying environment with a constant temperature. In this way, the agglomeration is effectively reduced and the nanoparticles are uniformly dispersed. In addition, the feasibility of large-scale preparation by reflux method was explored [48].

3. Modification of SnO_2/g-C_3N_4 heterojunction

In order to further enhance the photocatalytic performance of SnO_2/g-C_3N_4 heterojunction, some useful strategies have been developed, such as morphology control, defect introduction, and multiple structural optimization strategies.

3.1 Morphology control

Materials' morphology plays an essential role in their properties, so morphology control is particularly important for the SnO_2/g-C_3N_4 heterojunction photocatalyst. The desired photocatalytic efficiency and stability can be obtained by changing the morphology of SnO_2/g-C_3N_4, such as 0D/2D structure, 1D/2D structure, 2D/2D structure or other structures.

3.1.1 0D/2D structure

The nanosheet-structure g-C_3N_4 is more favored by researchers than the bulk g-C_3N_4. Because the two-dimensional structure has obvious advantages, such as reducing the transfer distance of photogenerated carriers, increasing the specific surface area, and enhancing the adsorption performance. Therefore, the construction of SnO_2/g-C_3N_4 with 0D/2D structure based on g-C_3N_4 nanosheets is an attractive subject, because it has a large number of point-to-face contacts that can provide fast charge transfer channels.

Generally, a crystal with critical size less than or equal to its exciton Bohr radius

can be called zero dimensional quantum dots (QDs). Different from traditional particles, QDs possess smaller particle size (1-10 nm), higher specific surface area, possible increased defect concentration and special quantum confinement effect. The quantum confinement effect plays a dominant role in the small size nanoparticles and has a strong impact on the electronic structure of semiconductors. It can change the spatial distribution and overlap of the wave functions of electrons and holes, and lead the original continuous energy level to a quantized energy level. The continuous optical transitions between the valence band and the conduction band also become discrete, which shows that the material properties are strongly dependent on size [49, 50]. Chen et al. [51] reported that SnO_2 nanoparticles from 13 nm to 3.0 nm and correspondingly the band gap increases from 3.5 eV to 4.0 eV. The quantum size effect leads to the broadening of band gap, and the effective band gap energy changes with the small size, as shown in Eq. (1). With the decreasing nanocrystal size, the binding energy of excitons generated by the recombination of electrons and holes have increased, and the quantized energy levels only allow transitions between energy levels with the same quantum number. More importantly, the energy required for transition increases with $1/\alpha^2$ (Eq. (2)), while the Coulomb force between electron and hole (assisted recombination) increases only with $1/\alpha$ (Eq. (3)). The resistance to electron-hole recombination is greater than the dynamic force when the size decreases. Therefore, the quantum confinement effect inhibits the electron-hole recombination to some extent [52].

$$E_g^{eff} = E_g + \frac{\hbar^2 \pi^2}{2\mu r^2} \quad (1)$$

$$E_{l,n}^{e,h} = \frac{\hbar^2 \phi_{l,n}{}^2}{2 m_{e,h} a^2} \quad (2)$$

$$e^2 / \in a \quad (3)$$

where r is the mean grain size, μ is the effective reduced mass (0.27 m_e for SnO_2), E_g refers to the bulk band gap energy (3.6 eV), and E_g^{eff} represents the effective band gap energy; l is the angular momentum quantum number, $m_{e,h}$ is the electron and hole

effective mass, *a* is the crystal radius, and $\phi_{l,n}$ is the n_{th} root of the spherical Bessel function. It has been demonstrated that the photocatalytic activity of SnO_2 QDs could be better than large particles [49, 53].

Therefore, the uniform dispersion of SnO_2 QDs on g-C_3N_4 nanosheets can effectively construct the heterojunction interface with a large number of 0D/2D point-to-face contacts, which can provide fast transport channel for facilitating electron-hole transfer and separation. So SnO_2 QDs/g-C_3N_4 has excellent photocatalytic performance due to the coefficient of quantum confinement effect and heterojunction interface. Fazal Raziq et al. [35] combined the thermally exfoliated g-C_3N_4 with SnO_2 QDs (Fig. 7 and 8, SnO_2 with small size of 3-4 nm) can degrade more than 90% RhB in 100 min, and the apparent rate constant of the composite (0.046 min^{-1}) is 460 times higher than pure SnO_2 (0.0001 min^{-1}). In addition, SnO_2 QDs with a size of less than 3 nm were prepared in the presence of g-C_3N_4 [54], and its MO degradation efficiency was 94% in 180 min under visible light. However, it is worth noting that there is no direct comparative study on the photocatalytic activity between SnO_2 QDs/g-C_3N_4 and SnO_2 large particles/g-C_3N_4. It is worth exploring in the future to visually highlight the influence of heterojunction interface and quantum confinement effect on photocatalytic performance.

3.1.2 1D/2D structure

One-dimensional nanomaterials (such as nanotubes, nanowires, nanofibers, nanorods, etc.) have the advantage of a large length-diameter ratio, which is conducive to long-distance charge transport and recycling [55]. And 1D/2D structure can be simply divided into vertical type and parallel type in appearance [56]. The 1D/2D heterostructure constructed by loading small-size 1D materials on 2D materials belongs to parallel type and has the obvious line-to-face contact. Compared with 0D/2D point-to-face contact, it has a larger heterojunction contact interface area and better charge transfer performance. For example, Wu et al. [57] loaded SnO_2 nanowires on P-doped g-C_3N_4（PCN） nanosheets by electrostatic self-assembly method to obtain SnO_2/PCN

(Fig. 9), which greatly improved the hydrogen evolution rate under visible light (2090 μmol h^{-1} g^{-1}) compared to PCN (132 μmol h^{-1} g^{-1}), and climbed to 12469 μmol h^{-1} g^{-1} in the presence of a small amount of Pt. This excellent photocatalytic hydrogen evolution performance is closely related to the 1D/2D heterojunction interface, which greatly improves the separation efficiency of photogenerated electrons and holes.

3.1.3 2D/2D structure

The 2D/2D structure has face-to-face contact interface, which theoretically has larger contact area and stronger interaction than 0D/2D point-to-face contact and 1D/2D line-to-face contact. It can maximize the merits of heterojunction interface for separating electrons and holes and show superior photocatalytic performance [58, 59]. Wang et al. [38] prepared 2D/2D SnO_2/g-C_3N_4 heterostructure by calcining melamine with the pre-prepared SnO_2 nanoflowers, in which the flower-like structure SnO_2 was formed by SnO_2 nanosheets (Fig. 10). The results show that the content of g-C_3N_4 precursor plays a controlling role in the morphology and size of heterojunction. When the content of g-C_3N_4 in the composite increased from 0 to 75%, the flower became more compact and smaller, and the surface area was larger. However, it is worth noting that the RhB degradation efficiency under visible light does not always increase with the g-C_3N_4 content, and SnO_2/50% g-C_3N_4 exhibits the highest photocatalytic rate is 0.0289 min^{-1}(Fig. 11). The potential reason is that excessive g-C_3N_4 destroyed the integrity of the flower-like structure, and the advantage of large contact area of the original layered 2D/2D heterostructure for face-to-face contact was constrained, which affects the optimization of carrier separation efficiency.

3.1.4 Other structures

The mainstream structure of the SnO_2/g-C_3N_4 system has been introduced, with g-C_3N_4 two-dimensional structure as the loading platform. In addition, there are other structures of SnO_2/g-C_3N_4.

Not only the 2D/2D structure can increase the contact area of the heterojunction, but the core-shell structure SnO_2@g-C_3N_4 heterojunction can also form face-to-face

contact. Core-shell structure is consisting of an inner core and an outer shell. The inner core is coated with a shell to obtain surface modification and improvement of the corrosion resistance and stability [60]. For SnO_2@g-C_3N_4, the main contribution of the core-shell structure is to increase the close contact area between SnO_2 and g-C_3N_4 as much as possible. For example, Shen et al. [20] obtained the SnO_2(core)@g-C_3N_4(shell) concentric spherical core-shell structure by one-step calcination of SnO_2 microspheres with urea(Fig. 12 and 13), and the apparent degradation rate constant of MO under visible light was 0.013 min^{-1}. The visible-light-driven g-C_3N_4 absorbed the light as the outer shell, and then the photogenerated electrons transfered to SnO_2 core through the heterojunction interface to achieve the purpose of electron hole separation. The morphology obtained by this well-designed coating process is more controllable than the uncertain and unpredictable process of random loading of SnO_2 on g-C_3N_4. Unfortunately, there are only a few reports on the core-shell structure of SnO_2@g-C_3N_4 at present. And many factors affecting the photocatalytic performance of the core-shell structure have not been studied in detail, including different synthesis strategies, the relative thickness and size of the core-shell, the integrity and uniformity of the shell coating, etc. In addition, there is a lack of other applications of SnO_2@g-C_3N_4 except dye degradation, which may be the direction of further research.

The bulk g-C_3N_4 also has its advantages, which could build a porous structure to promoting light absorption capacity, increasing specific surface area and enhancing transmission power. The SnO_2/g-C_3N_4 heterojunction of three-dimensional highly interconnected porous structure with abundant pores shows its unique advantages in photocatalytic performance. However, it should be pointed out that the formation of porous structure traditionally relies on special templates, which have obvious disadvantages of complex preparation process and high cost of template removal. In recent studies, SnO_2/g-C_3N_4 porous structure was successfully obtained by in-situ co-pyrolysis that using gaseous products generated from the decomposition of precursors. As a promising synthesis method, it can directly adjust the pore structure and density

of porous structure. For example, Chen et al. [44] synthesized SnO_2/g-C_3N_4 with a loose porous structure, which is different from the densely packed structure of bulk g-C_3N_4 (Fig. 14). According to the N_2 adsorption-desorption analysis of pore size distribution (PSD) curves (Fig. 15), the obtained SnO_2/g-C_3N_4 has significant macroporous structure and large surface area. With the increase of gas released from the precursor, the amount of small pores has increased and the amount of large pores has decreased. When the precursor ratio of SnO_2 to g-C_3N_4 is 1:20, SnO_2/g-C_3N_4 has the highest specific surface area (44.342 $m^2 \cdot g^{-1}$) and total pore volume (2.638 $cm^3 \cdot g^{-1}$), which showed the best visible light degradation performance of methyl blue (MB) and good cycle stability. Moreover, Seza et al. [45] obtained SnO_2/g-C_3N_4 with nanoscale pores for realizing photoelectrochemical water splitting, which shows high specific surface area (195 $m^2 \cdot g^{-1}$) and photocurrent density (33 $mA \cdot cm^{-2}$).

Of course, other morphologies of g-C_3N_4 also have photocatalytic potential, like granular g-C_3N_4. For example, the SnO_2/g-C_3N_4 heterojunction with narrow particle size distribution of SnO_2 was successfully prepared without any additional stabilizer, because the g-C_3N_4 particles serve as a template [47]. And the average particle size of SnO_2 prepared in the presence of g-C_3N_4 particles nearly 4 nm, which is smaller than SnO_2 (14 nm) prepared in the absence of g-C_3N_4. It can be explained by multiplicative mechanism [61], the dynamic light scattering (DLS) result shows that SnO_2 nanoparticles settle in the micropores inside g-C_3N_4 particles during the formation of composite, which successfully restricts the growth and aggregation of SnO_2. Meanwhile, the size of SnO_2/g-C_3N_4 particles increases from 763 nm of original g-C_3N_4 to 1316 nm. Moreover, the conduction band and valence band positions of the g-C_3N_4 particles (-1.26 eV and 1.60 eV, respectively) were similar to the exfoliated g-C_3N_4 nanosheets, which ensure the visible light absorption capacity of SnO_2/g-C_3N_4 heterojunction photocatalyst.

3.2 Defect introduction

Defect introduction is an eye-catching strategy to adjust the photocatalytic performance of SnO_2/g-C_3N_4 heterojunction. The purpose of introducing defects into

the crystal lattice is to affect the surrounding electronic structure and cause some favorable transformation.

3.2.1 Heteroatom doping

Heteroatom doping is an effective way to modify semiconductor materials, because the electronic structure of the material will change at the micro level, which will affect the macro performance. Here, dopants can be simply divided into n-type doping and p-type doping, also known as electron donor and electron acceptor. Heteroatoms become substitutional atoms or interstitial atoms in the original lattice, forming new local energy levels in the forbidden band, which can change the band gap of the material or the position of CB or VB. The current research mainly includes two directions:

The most important purpose of doping SnO_2 is to solve the problem that the wide band gap can only absorb ultraviolet light, so as to achieve visible light absorption. For example, the degradation efficiency of RhB, CO_2 reduction, and isopropanol (IPA) oxidation under visible light of Sb-SnO_2/g-C_3N_4 were significantly enhanced [62, 63]. Due to the difference in valence electrons between Sb ($5s^2$ $5p^3$) and Sn ($5s^2$ $5p^2$), when Sb is used as a donor dopant to replace Sn atom in SnO_2, an extra weakly bonded electron can be released into the conduction band. At this time, there is a vacancy state in the local energy level near the bottom of CB due to Sb doping, which can also capture the photogenerated electrons excited from the valence band. In brief, the results show that the bottom position of CB moves down, which is mainly attributed by O 2p and Sb 5s as well as a small amount of Sb 5p, Sn 5s and Sn 4d. The bandgap reduction caused by the movement of the conduction band minimum (CBM) has been confirmed by theoretical calculation [64] and experiment [63] (Fig. 16 and 17). Nevertheless, excessive doping may cause surface defects to act as recombination centers of photogenerated electrons and holes, which is harmful to photocatalytic activity [62].

It is worth mentioning that doping with g-C_3N_4 can further expand the visible light absorption range. The degradation efficiency of SnO_2/S doped g-C_3N_4 synthesized

through in-situ thermal condensation is significantly better than that of S-g-C_3N_4 and SnO_2 under visible light [65]. It is attributed to the co-effect of heterojunction and doping, which promote the transmission of photogenerated electrons and enhance the light response range. During the in-situ condensation, a very small part of the S atoms substituted for O in the SnO_2 lattice (about 0.34 at%) can be ignored. Most of the doped S atoms substituted N in g-C_3N_4 lattice, forming C-S bond in the structure (Fig. 18). The n-type doping of S forms a local energy level near the bottom of the CB of g-C_3N_4, which reduces the band gap of g-C_3N_4 to 2.55 eV. Moreover, F. Raziq et al. [66] synthesized SnO_2/B,P co-doped-g-C_3N_4 composite as an efficient photocatalyst for reducing CO_2 and degrading pollutants (such as phenol and acetaldehyde) (Fig. 19). The results of Bruer nuclear magnetic resonance (NMR) and first density functional theory (DFT) [67] confirmed that both B and P replace C atoms in g-C_3N_4 lattice, in which P atoms were connected with three N atoms at the original position of carbon or at the interval of carbon to form P-N bonds (Fig. 20). In detail, P substituted C is n-type doping and B substituted C is p-type dopant, which forms impurity energy levels near the bottom of CB and the top of VB respectively. The simultaneous modulation of semiconductor CB and VB significantly reduces the band gap of g-C_3N_4 from 2.7 eV to 2.2 eV, and the corresponding visible light absorption edge increases from 460 nm to 550 nm.

In addition, co-doping, especially donor-acceptor co-doping, can provide charge compensation between the donor and the acceptor to maintain the electrical neutrality of the entire system. Co-doping facilitates the separation of carriers and reduces the recombination of electron-hole pairs caused by isolated energy level of single doping. In short, the suitable doping concentration is a prerequisite. Correspondingly, doping can produce shallow or deep doping levels. The former has a weak binding force and easy to be ionized, which is an effective doping. On the contrary, deep doping level has a strong binding force and is difficult to ionize, which cannot play an ideal role. The Fermi-Dirac distribution describes the probability that electrons occupy a certain

energy level at a certain temperature. At higher temperatures, the conduction band energy level is likely to be occupied, and the trap state energy levels tend to provide electrons to the conduction band. The detection of free electrons generated in the trap state can confirm that an occupied energy level in the forbidden band. Because the free electrons generated by CB and shallow trap state contribute to infrared absorption at higher temperatures, Zhang et al. [68] detected the shallow trap level of Cu-doped TiO_2 by high pressure temperature-programmed in-situ Fourier Transform Infrared Diffuse Reflection Spectroscopy (FTIR-DRS). The electrons in the shallow trap state can be thermally excited into the conduction band at room temperature, which can prove that the energy gap between the CBM and the trap state is small. Faisal S. et al. [69] used deep-level transient spectroscopy (DLTS) to investigate the shallow trap levels in In-doped TiO_2, and DLTS can also provide information on defects parameters, including energy, capture cross section and concentration. In addition, the photoluminescence (PL) spectrum can also characterize the trap state energy level position in the forbidden band. So, how to achieve shallow doping? First, in order to find a theoretically feasible shallow doping, the ionization energy of the doping atoms can be calculated. For example, He et al. [70] used first-principles calculations based on plane wave pseudopotentials and density functional theory (DFT) to study the generation energy and electronic structure of Mg doping in SnO_2. Mg-doped SnO_2 has p-type conductivity, in which the doped energy level is about 0.5 eV higher than the Fermi level, and the ionization energy of Mg is about 21 meV, confirming that Mg doping in SnO_2 has a shallow level. Du et al. [71] compared the electronic structure of III-group atoms (including Al, Ga, In) doped in SnO_2. And density of states calculation result shows that the doping of III-group atoms produces acceptor energy levels. The ionization energy of substitutional In in SnO_2 is the smallest (0.06 eV), so its acceptor energy level in SnO_2 is the shallowest under the same doping concentration. In practice, the position of the doping energy level can be adjusted by controlling the doping concentration. Li et al. [72] confirmed that light Ni doping can form substitutional Ni in CdS and is

related to the shallow surface states, while heavy Ni doping can form interstitial Ni in CdS and is related to the deep surface states. The photoluminescence spectrum shows that the 2.17 eV peak correlated with substituted Ni is located at 0.29 eV below the CB, and the 1.8 eV peak correlated with the interstitial Ni is located at 0.65 eV below the CB. Surface photovoltage (SPV) spectroscopy obtains the maximum response intensity in CdS with 2% Ni content, but the response intensity decreases when the Ni content continues to increase, which is related to the interstitial Ni as a recombination center under heavy doping. Under heavy doping (10% Ni-CdS), the transient photovoltage (TPV) spectroscopy signal attenuation is related to the recombination of the carrier relaxation to the deep surface states. In addition to changing the doping concentration, currently H doped TiO_2 introduces a shallow doping level higher than the deep level of the oxygen vacancy, and the electrons captured by the deep energy level can be thermally excited to the shallow doping level [73]. The reversed double-beam photoacoustic spectroscopy (RDB-PAS) confirmed that doped H is a shallow level at the bottom of the conduction band, and the calculation result shows that H doped SnO_2 also exists as a shallow level [74].

3.2.2 Vacancy introduction

(1) Oxygen vacancy in SnO_2

The introduction of oxygen vacancies into SnO_2 is to modulate the energy band structure and enhance its light absorption range. It is also a very favorable way to improve the overall photogenerated carrier yield of SnO_2/g-C_3N_4 heterojunctions. In generally, Sn^{4+} of the precursor is reduced to Sn^{2+} (Gibbs free energy $\Delta_r G_m^0$ =-55.96 kJ·mol^{-1}, which is a thermodynamic favorable process) or partial oxidation of Sn^{2+} to Sn^{4+} to obtain non-stoichiometric self-doped SnO_{2-x}. The main achievement is to dope Sn^{2+} into the SnO_2 lattice to partially replace the original Sn^{4+} position. With the substitution of this heterovalent ion, oxygen vacancies are generated due to its lowest formation energy and the requirement of electrical neutrality balance. Oxygen vacancies have the lowest formation energy, compared to other defects such as

interstitial oxygen O_i, tin vacancy V_{Sn}, interstitial tin Sn_i [75]. Moreover, compared with the heteroatom doping, the self-doping can better maintain the integrity and stability of the crystal structure. Because the radius and electronegativity difference between self-doping ion and original lattice ion is smaller, it is possible to achieve high concentration of self-doping [76-78].

The oxygen vacancies in the lattice can improve the photocatalytic performance by adjusting the electronic structure. According to the classical theory, self-doped SnO_{2-x}, a non-stoichiometric compound with anion vacancy, produces excess free electrons in the lattice while Sn^{2+} partially replaces Sn^{4+}. However, it is easy to be bound by the positive charge centers formed by oxygen vacancies, thus forming some color centers that can absorb light of certain wavelengths, which makes the pure SnO_2 change from white to yellow or even deep yellow with the increased concentration of oxygen vacancy. The possible defect equations are as follows (Eq. (4) and (5)):

$$Sn_{Sn}+2O_o \rightarrow Sn''_{Sn}+V_O^{\cdot\cdot}+O_2 \quad (4)$$

equivalent to:

$$O_o \rightarrow V_O^{\cdot\cdot}+\frac{1}{2}O_2+2e' \quad (5)$$

Both experimental characterization and theoretical calculation results can confirm that oxygen vacancy forms a new defect energy level in the SnO_2 bandgap. From the perspective of solid physics and solid chemistry energy band theory, it can be ionized at room temperature and release electrons into CB as a shallow donor level. Generally, the position of the defect energy level in the forbidden band should be close to the bottom of the conduction band [79]. But in fact, there are different research conclusions [39]. For example, Anuchai et al. [76] combined density functional theory calculations with VB-XPS and UV-vis DRS spectra analysis, which reveals that the defect energy level formed by oxygen vacancy is located above SnO_2 VB and partially overlapped. As a result, the width of VB becomes wider and the top of VB shifts upward, and the band tail state appears below CB (Fig. 21). Eventually the oxygen vacancy SnO_2 band gap is reduced, and the corresponding light absorption is increased. From the

perspective of atomic orbitals, SnO_2 valence band mainly consists of p orbitals, and the conduction band mainly consists of s and p hybrid orbitals. The new defect energy levels may be attributed to the results of Sn^{2+} 5s and O 2p orbital hybridization [80].

Based on the above results, visible-light-driven SnO_{2-x} was further coupled with g-C_3N_4 to construct SnO_{2-x}/g-C_3N_4 heterojunction photocatalyst. Under visible light, the SnO_{2-x}/g-C_3N_4 heterojunction photocatalyst has excellent performance and high PEC and PC activity [46], which can realize the degradation of tetracycline (TC) and RhB, the removal of antibiotics and the inactivation of E. coli [79], reduction of CO_2 [39], etc. The oxygen vacancy concentration can be directly adjusted by controlling the Sn^{2+} doping amount and indirectly adjusted by changing the grain size[51]. However, it is worth noting that the SnO_2 grains are small enough (less than twice the Debye length) so that the oxygen vacancies act as electron collectors. The local photogenerated electrons captured by the oxygen vacancies in SnO_2/g-C_3N_4 are not conducive to hydrogen production from water splitting. Reduction of hydrogen ions to hydrogen requires the contribution of conduction band free electrons. But the competitive migration mechanism of photogenerated electrons between the conduction band and oxygen vacancies (Fig. 22) has a negative effect on photocatalytic hydrogen evolution. Fortunately, this localized electron is still in an excited state different from the valence band electron. It can be re-excited to the SnO_2 conduction band under infrared light through the complex phonon electron interaction produced by lattice vibration, and can be reused in the hydrogen evolution process to compensate for its possible adverse effects.

(2) Nitrogen vacancy in g-C_3N_4

The effect of nitrogen vacancy in g-C_3N_4 is similar to that of oxygen vacancy in SnO_2, which changes the electronic structure and band position of the material by introducing a defect energy level into the forbidden band. The new defect level formed by nitrogen vacancy usually exists near the bottom of g-C_3N_4 conduction band as a shallow donor level, which makes the band gap narrower and broadens the visible light

absorption range [81]. The new defect level of nitrogen vacancy can capture photogenerated carriers [82], and effectively inhibit the recombination of photogenerated electrons and holes [83]. In order to explore the specific location of the nitrogen vacancy V_N in the g-C_3N_4 framework, Xu et al. [84] revealed that the nitrogen vacancy was mainly generated at the N_{3C} (N-$(C)_3$) site of the heptaazine ring, which slightly reduced bandgap from 2.76 eV of the bulk g-C_3N_4 (BCN) to 2.71 eV, and its CB (-0.96 eV) position moved up 0.10 eV than BCN (-1.06 eV). The nitrogen-rich vacancy g-C_3N_4 can inactivate E. coli under visible light, and the degradation efficiency of methylene blue, magenta and bisphenol A are 3.1, 2.5 and 1.6 times that of BCN, respectively. It can be reasonably predicted that constructing such a defect-rich g-C_3N_4/SnO_2 heterojunction may achieve better photocatalytic performance, but the literature is temporarily lacking.

(3) Double defect heterojunction

It is possible to combine SnO_2 with oxygen vacancies and g-C_3N_4 with nitrogen vacancies to construct a double defect heterostructure, which could also be a promising way to improve photocatalytic performance. Although there are no direct reports yet on the study of SnO_2/g-C_3N_4 double defect heterostructure, it is worth noting that Gao et al. [85] studied the hydrogen evolution performance of defect-rich TiO_2/defect-rich g-C_3N_4 nanosheets (DR-TiO_2/DR-CNNS) heterostructure, and the maximum hydrogen evolution rate (651.79 $\mu mol \cdot h^{-1}$) higher than other reported g-C_3N_4 based composites and single defect DR-TiO_2/CNNs (293.48 $\mu mol \cdot h^{-1}$) and TiO_2/DR-CNNs (368.59 $\mu mol \cdot h^{-1}$), as shown in Fig. 23. The improved hydrogen evolution performance can be attributed to the double defect effects, which can provide more reactive sites for photocatalytic hydrogen evolution [86]. The results of time-resolved PL spectroscopy (TRPL) show that the double defect DR-TiO_2/DR-CNNS composite has a higher photogenerated charge lifetime than the single defect system DR-TiO_2/CNNs (τ=3.125 ns) and TiO_2/DR-CNNs (τ=3.416 ns), which provides photogenerated electrons for hydrogen evolution. The above results provide a helpful insight for the construction of

a double defect heterojunction between oxygen-rich vacancy SnO_2 and nitrogen-rich vacancy g-C_3N_4. Therefore, we boldly predict that double defect SnO_2/g-C_3N_4 heterojunction may offer surprising results and have great application potential in photocatalytic reaction, which could be a subject worthy of further research.

Moreover, the mechanism of defects in heterojunction materials needs to be further studied. In addition to oxygen vacancy and nitrogen vacancy, the effect of other types of defects on photocatalytic performance can also be studied in the future.

3.3 Multiple structural optimization strategies

Although the photocatalytic performance of SnO_2/g-C_3N_4 heterojunction is much higher than that of pure SnO_2 or pure g-C_3N_4, there is still room for improvement. Apart from morphology control and defect introduction, there are multiple structural optimization strategies to enhance SnO_2/g-C_3N_4 photocatalytic performance, including co-catalyst loading, and ternary heterostructure, etc.

3.3.1 Co-catalyst loading

Doping will introduce impurities into the lattice, which is harmful to the crystallinity. Different from doping, noble metal nanoparticles as co-catalysts (such as Ag, Au) can be loaded on SnO_2/g-C_3N_4 surface without destroying the crystallinity, which can promote the migration and separation of photogenerated carriers and prolong their lifetime [87]. Noble metals have good physical and chemical stability and excellent anti-corrosion properties, and are usually deposited on the surface of SnO_2/g-C_3N_4 by photochemical reduction. However, the toxic reagents used in traditional chemical reduction are potentially harmful to the natural environment. According to recent reports, Ag nanoparticles can be successfully deposited on SnO_2/g-C_3N_4 surface by biofilm reduction [88], which should be the general trend in the future.

There are two main effects of loading noble metals on SnO_2/g-C_3N_4: (1) Increase the electron density of the photocatalytic reaction due to the unique surface plasmon resonance (SPR) effect, that is, noble metals can be excited by light to generate hot electrons; (2) Acting as an electron transmission bridge between g-C_3N_4 and SnO_2 to

promote rapid electron migration to reduce recombination. This ternary composite has good performance in photocatalytic degradation of pollutants, CO_2 conversion and hydrogen production from water splitting [27, 87-89]. It is found that the details of the electron transfer path are as following: under visible light irradiation, g-C_3N_4 generates photogenerated electrons and noble metal nanoparticles generate hot electrons (Fig. 24), the photocurrent below 470 nm can be attributed to g-C_3N_4, while the photocurrent above 470 nm comes from Au, and the photocurrent above 520 nm is ignored due to low energy [27]. Because the work function of metal is greater than g-C_3N_4, photogenerated electrons tend to transfer from g-C_3N_4 CB to the surface of noble metal [90][90]. In addition, the photogenerated electrons of g-C_3N_4 are also transferred to SnO_2 CB through the heterojunction interface, and the hot electrons generated by Ag or Au are also transferred to SnO_2 CB. The purpose of electron-hole pair separation is successfully achieved (Fig. 25). It is also worth mentioning that the original SnO_2 CB position is not conducive to hydrogen evolution. After coupling g-C_3N_4 and loading noble metals, the Fermi levels of the semiconductors are aligned with the Fermi levels of the metals. Due to the redistribution of the interface charge, the upward movement of SnO_2 CB is more suitable for photocatalytic hydrogen production. Generally, the more precious metals loaded within a controllable range, the better the photocatalytic performance of the ternary composites [88].

3.3.2 Ternary heterostructure

A ternary heterostructure also can be constructed by coupling a new semiconductor component with the SnO_2/g-C_3N_4 system to build more contact surfaces, which can provide a new transmission channel to photogenerated charge carriers and realize multi-level charge transport. According to the energy level matching between different semiconductors, it is possible that each semiconductor in the ternary heterostructure contacts with the other two semiconductors to form heterojunction interface, or only a part of the components form heterojunction. For example, Yang et al. [91] obtained g-C_3N_4/SnS_2/SnO_2 ternary heterostructure with the excellent photocatalytic performance

of Cr(VI) reduction under visible light. SnS_2 is added to SnO_2/g-C_3N_4 because of its advantages such as suitable band gap, large specific surface area, and controllable morphology. In the ternary heterostructure (Fig. 26), each component (g-C_3N_4, SnO_2 and SnS_2) can form a heterojunction interface with the other two. The results show that g-C_3N_4 and SnS_2 can be excited by visible light, which have increasing photogenerated carriers compared to only excited g-C_3N_4. Due to the effects of heterojunction and built-in electric field (BIEF), the electron transfer path is as follows: g-C_3N_4 CB → SnO_2 CB, g-C_3N_4 CB → SnS_2 CB → SnO_2 CB, SnS_2 CB → SnO_2 CB. The transfer path of photogenerated hole may be: SnS_2 VB → g-C_3N_4 VB. In a word, photogenerated electrons accumulated on SnO_2 CB successfully reduced Cr (VI) to Cr (III), while photogenerated holes accumulated on g-C_3N_4 CB. In short, the g-C_3N_4/SnS_2/SnO_2 ternary heterostructure effectively separates charge carriers.

More interestingly, Yuan et al. [92] added diatomite, a porous silicate structure, into SnO_2/g-C_3N_4 to construct SnO_2/g-C_3N_4/diatomite ternary composites (Fig. 26 (d)), which show excellent photocatalytic performance for Cr (VI) reduction in the presence of citric acid. The existence of diatomite effectively avoids the excessive accumulation and aggregation of SnO_2/g-C_3N_4, and its pore structure provides rich adsorption and reaction sites. In particular, the Si-O group on the surface of diatomite is positively charged after protonation in citric acid atmosphere, which can adsorb Cr anion through electrostatic attraction. The Cr (VI) reduction efficiency was significantly improved, which was 98.0% at 150 min.

It is also worth mentioning that SnO_2/g-C_3N_4/TiO_2 nanotube/Ti nanoplate[93] composites have been prepared with excellent degradation of E.coli and 2-propanol under visible light. Similarly, in SnO_2-ZnO/g-C_3N_4 ternary composites [94], the photogenerated electrons transfer from g-C_3N_4 CB to ZnO and finally accumulate on SnO_2 CB, while the migration path of photogenerated holes is opposite. There is no doubt that the improved multi-level transport of charge carriers in a multiple heterojunction is beneficial to prolong the life of electrons and significantly inhibits

electron-hole pair recombination [95]. Compared with the SnO_2/g-C_3N_4 binary heterojunction, the photocatalytic ability is further improved in multiple composites.

Different morphologies, modification methods and experimental conditions will affect the photocatalytic performance of SnO_2/g-C_3N_4 heterojunction. Table 2 has summarized the photocatalytic performance of SnO_2/g-C_3N_4 heterojunction and its potential applications.

4. Mechanisms and Applications

Photocatalysis is an excellent tool for environmental remediation and energy conversion. Here, the possible photocatalytic mechanisms and applications of SnO_2/g-C_3N_4 heterojunction are summarized. In addition, theoretical calculations and some new techniques can be used to detect the specific process of SnO_2/g-C_3N_4 interface charge transfer.

4.1 Mechanisms

Heterojunction as a useful modification method has become a research hotspot. The most important contribution of the SnO_2/g-C_3N_4 heterojunction in photocatalytic performance is the separation of photogenerated electrons and holes through the staggered band location between SnO_2 and g-C_3N_4. The mechanism of SnO_2/g-C_3N_4 heterojunction has been developed rapidly, including the traditional type II heterojunction, Z-scheme heterojunction, S-scheme heterojunction, etc.

First of all, type II heterojunction of SnO_2/g-C_3N_4 effectively alleviates the weak redox ability of single photocatalyst. And the typical charge transfer mode of SnO_2/g-C_3N_4 II heterojunction is that the photogenerated electrons transfer from the negative CB of g-C_3N_4 to SnO_2 CB driven by the work function (Fig. 8), and the photogenerated electrons and holes are separated successfully in space. In our previous work, SnO_2/g-C_3N_4 composite was constructed and confirmed to be type II heterojunction by experiment and theoretical calculation [96]. According to the first-principles calculation, the work functions of SnO_2(110) and g-C_3N_4 nanosheets (CNNSs) are 6.729 eV and 4.446 eV respectively, and the difference of Fermi energy level can drive electrons

transfer from CNNSs to SnO_2. The average charge density difference between SnO_2(110) and CNNSs in the Z direction describes the charge movement at the heterojunction interface (Fig. 27), which is positive on the SnO_2(110) side and negative on the CNNSs side, indicating that electron depletion layer and accumulation layer are formed in the space charge region of CNNSs and SnO_2(110) respectively. The calculation results of the density of states (Fig. 28) show that the bottom of SnO_2(110) CB is determined by the O p orbital, while the top of VB is mainly occupied by the O p and Sn 4s orbitals. In CNNSs, both the bottom of the CB and the top of VB are determined by the N 2p and C 2p orbitals. For SnO_2(110)/CNNSs, the top of VB is composed of N 2p and C 2p, and the bottom of CB is composed of O p orbitals. In addition, the theoretical calculation results are consistent with the charge transfer obtained by XPS, which supports the mechanism of SnO_2/g-C_3N_4 II heterojunction. At present, SnO_2/g-C_3N_4 type II heterojunction has been extensively studied [97-99], but the improvement of its electron hole separation efficiency is at the expense of redox capacity, which may not meet the redox potential of some reactions. And the existing electrons on SnO_2 CB will hinder the continuous transfer of g-C_3N_4 electrons.

The Z-scheme heterojunction has a stronger driving force for specific reactions because it retains high redox ability while successfully separating photogenerated electrons and holes [100]. Assuming that the SnO_2/g-C_3N_4 heterojunction follows the Z-scheme mechanism, the photogenerated electrons on the SnO_2 CB will directly or indirectly recombine with the holes of the g-C_3N_4 VB. Therefore, the premise of the Z-scheme heterojunction is that both SnO_2 and g-C_3N_4 semiconductors generate electron-hole pairs under light excitation, otherwise the Z-scheme mechanism will fail. For example, Fe-doped SnO_2/g-C_3N_4 [101] has a Z-scheme charge transfer pathway under simulated sunlight, in which Fe^{3+} doped on the surface of SnO_2 can be reduced to Fe^{2+} by e^- of the Fe-SnO_2 CB, and O_2 in the photocatalytic system can oxidize Fe^{2+} to Fe^{3+} and then transform into superoxide radicals. The Fe^{3+}/Fe^{2+} cycle promotes the successful separation of photogenerated electrons and holes of SnO_2/g-C_3N_4, which is

a key charge transfer medium for indirect Z-scheme heterojunction. In order to construct SnO_2/g-C_3N_4 Z-scheme heterojunction under visible light, the band structure of SnO_2 can be adjusted by doping or defect levels to achieve visible light response, and then coupled with g-C_3N_4 is a fruitful way. Bao et al. [102] designed a defective flower-like SnO_2/g-C_3N_4 Z-scheme heterojunction, in which both defective SnO_2 (2.64 eV) and g-C_3N_4 (2.78 eV) have visible light absorption capacity. In addition, the electrons of the defect SnO_2 CB can oxidize Sn^{4+} to Sn^{2+}, and the holes of g-C_3N_4 VB contribute to the reduction of Sn^{2+} to Sn^{4+}. Accordingly, the redox pair of Sn^{4+}/Sn^{2+} acts as the charge transfer channel of the SnO_2/g-C_3N_4 indirect Z-scheme heterojunction system under visible light (Fig. 29). The indirect Z-scheme heterojunction requires a transmission medium which is detrimental to its long-term stability. From the dynamic perspective, the photogenerated electrons on g-C_3N_4 CB have a stronger captured power and a larger potential difference with the transmission medium, which may compete with the Z-scheme mechanism. Therefore, the SnO_2/g-C_3N_4 direct Z-scheme heterojunction without transmission medium is superior to the indirect Z-scheme heterojunction (Fig. 30). He et al. [39] confirmed that SnO_{2-x}/g-C_3N_4 direct Z-scheme heterojunction according to the free radical capture experiment, and photogenerated electrons with stronger reduction ability could satisfy the dynamic requirements of CO_2 reduction with good stability.

In order to give a more detailed and standardized interpretation of Z-scheme heterojunction, a novel S-scheme heterojunction emerged recently [103, 104]. Before contact, the work function of reduction photocatalyst g-C_3N_4 is smaller than that of oxidation photocatalyst SnO_2. After contact, electrons tend to actively flow from g-C_3N_4 to SnO_2 until their Fermi levels are in the same position. This process naturally produces band bending to hinder the continuous flow of electrons. As a result, an electron depletion layer is formed in the space charge region near g-C_3N_4, and an electron accumulation layer is formed on the SnO_2 side, thus establishing a built-in electric field at the interface. At the interface of SnO_2/g-C_3N_4, the electrons of SnO_2 CB

are combined with holes of g-C_3N_4 VB under the synergistic effect of band bending, built-in electric field and Coulomb gravity. The stronger redox capacity of g-C_3N_4 photogenerated electrons and holes of SnO_2 in the heterojunction system are expected to be used for photocatalytic. Viet van Pham et al. [105] considered that the obtained SnO_2/g-C_3N_4 belongs to S-scheme charge transfer mechanism through density functional theory calculation, free radical capture experiment and ESR results. Specifically, the calculated work functions of the n-type semiconductors SnO_2 and g-C_3N_4 are consistent with the S-scheme construction conditions, which are 4.65 eV and 6.65 eV, respectively. Assuming that the interface charge transfer conforms to the type II heterojunction, the electrons of SnO_2 CB and the holes of g-C_3N_4 VB cannot meet the production conditions of active species $\cdot O_2^-$ and ·OH, which contradicts the experimental results. Based on the above results, it is concluded that obtained SnO_2/g-C_3N_4 belongs to S-scheme heterojunction (as shown in the Fig. 31), and the stronger photogenerated electrons of g-C_3N_4 CB and holes of SnO_2 VB contribute to the generation of $\cdot O_2^-$ and ·OH, respectively.

4.2 Applications

4.2.1 Environment remediation

The applications of SnO_2/g-C_3N_4 photocatalyst in environmental remediation include degradation of pollutants (organic dyes, antibiotics, heavy metal ions), sterilization, air purification (removal of NO), etc.

The treatment of industrial and medical wastewater is a perplexing problem, which may be solved by photocatalysis. Firstly, the semiconductor photocatalyst generates electrons and holes in the CB and VB respectively under light excitation, and then the electrons and holes transfer to the surface of the photocatalyst and react with the adsorbed molecules to generate active free radicals, which can act on the removal process of pollutants (as shown in Eq. (6) to (9)). Due to surface reaction is rate-limiting step of photocatalytic process on time scale, it is increasingly recognized that pollutant removal is a synergistic contribution of adsorption and photocatalysis. The π-π conjugation on the surface of g-C_3N_4 can effectively adsorb organic dye molecules [29].

And Mohammad et al. [34] studied the effect of adsorption efficiency on photocatalytic degradation performance to confirm the adsorption-assisted photocatalytic degradation process. Moreover, the influence of solution pH in the photocatalytic process cannot be ignored [106]. Li et al. [107] analyzed the effect of initial pH on adsorption in detail. When the pH is greater than the zero potential of Carbon dots/g-C_3N_4/SnO_2 (3.64), the surface of the catalyst is negatively charged, and when the pH is less than the dissociation constant of Indomethacin (IDM) (4.5), IDM exists in the solution as a cation. Therefore, the optimum pH range for photocatalysis is 3.64-4.5, and the electrostatic attraction between the negatively charged surface of the photocatalyst and the IDM cation can promote the adsorption process. It is well known that photocatalysis can gradually decompose and mineralize pollutant molecules and eventually transform them into small molecules such as CO_2 and H_2O, which are harmless to the environment and organisms. The total organic carbon removal experiment showed the photocatalytic mineralization effect of IDM. According to the HRAM LC/MS/MS system, IDM's mineralization intermediates and possible conversion paths were analyzed in detail. After illumination for 80 min, the degradation rate of IDM was as high as 90.8%, and TOC removal rate was 29.4%, indicating that IDM molecules have been cleaved but most of them exist in the solution as more stable intermediates, which are not completely transformed into CO_2 and H_2O. After prolonged illumination time, the intermediates continued to open the ring and mineralize until they were completely transformed into CO_2 and H_2O, as shown in the Fig. 32. This method can be used as a reference for the analysis of photocatalytic degradation of other pollutants such as RhB[108], MB[109], MO, crystal violet [33], Congo red [34] and TC [79] by SnO_2/g-C_3N_4. Photocatalysis can also reduce toxic heavy metal ions Cr(VI) to non-toxic Cr(III)[91, 110]. There are two main ways: (1) direct reduction by photogenerated electrons, and (2) reduction by superoxide radicals. Because Cr(VI) often exists in solution as $Cr_2O_7^{2-}$, the reduction potential of $Cr_2O_7^{2-}/Cr^{3+}$ (+1.33 eV vs.NHE, pH=7) is much higher than that of $O_2/\cdot O_2^-$ (-0.33 eV vs.NHE, pH=7). Therefore, it is

considered that direct reduction of Cr(VI) by photogenerated electrons is a more competitive way in thermodynamics [111].

$$SnO_2/g\text{-}C_3N_4 + hv \rightarrow e^- + h^+ \quad (6)$$

$$e^- + O_2 \rightarrow O_2^-,\ O_2^- + H_2O \rightarrow HO_2^- + OH^- \quad (7)$$

$$HO_2^- + H_2O \rightarrow H_2O_2 + \cdot OH,\ H_2O_2 \rightarrow 2\cdot OH \quad (8)$$

$$h^+/O_2^-/\cdot OH + \text{pollutants} \rightarrow CO_2 + H_2O \quad (9)$$

Microorganisms in water also have potential hazards, and photocatalysis can be used for sterilization [79, 93]. The specific process is as follows: Photogenerated carriers generate active free radicals with high energy (e.g. ·OH is 120 kcal·mol^{-1}), which basically destroy bacterial cell wall and cell membrane. Then the free radicals will enter the cell and destroy the hydrogen bond (3.1-7.2 kcal·mol^{-1}) of the double-helical structure of DNA to inhibit DNA replication. Active free radicals can also decompose the disulfide bond (50.2 kcal·mol^{-1}) of functional macromolecular proteins and change the protein structure. In general, photocatalytic sterilization can be realized by destroying the cell structure and gradually disrupting cell metabolism. In addition, Chen et al. [112] evaluated the difference in the sterilization performance of Fe-SnO_2/g-C_3N_4 against E. coli and S. aureus. As a result, Fe-SnO_2/g-C_3N_4 has broad-spectrum antibacterial properties, and its sterilization activity of E. coli (80.9%) under natural light for 1 h was higher than that of S. aureus (59.5%). As a member of Gram-positive bacteria, S. aureus has a thick cell wall and the tight tissue intertwined with reticular molecules can resist the invasion of active free radicals. The performance of photocatalytic inactivation of E. coli is higher than S. aureus because of its thinner cell wall as Gram-negative bacteria. Fig. 33 shows that the original E. coli cells are complete, smooth and rod-shaped, while S. aureus cells are neat and clear and spherical, and some cells are broken under the photocatalytic of Fe-SnO_2/g-C_3N_4. Therefore, photocatalysis has a good potential for application to sterilization.

In addition to water pollution, air pollution such as the release of NO also produces a series of problems. And photocatalytic removal of NO produced toxic NO_2 by-

products will also cause more serious environmental problems. Therefore, it is necessary to consider the inhibition of NO_2 while photocatalytic removal of NO with SnO_2/g-C_3N_4. In addition, the dynamic process of photocatalytic oxidation of NO can be studied by in-situ Fourier transform infrared spectroscopy [113]. Fig. 34(a) shows the adsorption process under dark conditions, the adsorption bands at 1089 cm^{-1}, 1048 cm^{-1} and 1013 cm^{-1} belong to the physical adsorption of NO, cis-N_2O_2 and trans-N_2O_2 on the surface of SnO_2/g-C_3N_4, respectively. Fig. 34(b) shows that with the increase of visible illumination time, the peak of NO decreased gradually, and the adsorption band of N_2O_4 at 920 and 893 cm^{-1} also minished, indicating that SnO_2/g-C_3N_4 can effectively remove NO and significantly inhibit the generation of toxic NO_2 under illumination conditions. The SnO_2/g-C_3N_4 obtained by Pham Van Viete et al. [114] can remove 35% of NO under visible light irradiation for 30 min, and the NO_2 generation rate is limited to 2%, which is much lower than the NO_2 generation rate of pure g-C_3N_4 (12%). During the photocatalytic removal of NO, superoxide radical can oxidize NO to NO_3^- instead of NO_2 and photogenerated holes can convert NO into N_2O (1.03 eV), HNO_2 (0.99 eV), and HNO_3 (0.94 eV).

4.2.2 Energy conversion

Solar energy is a fascinating resource. However, solar energy has periodic and discontinuous problems, so the efficient use of solar energy is an eternal topic. For example, SnO_2/g-C_3N_4 photocatalyst has been widely used in energy conversion, which can convert solar energy into chemical energy by reducing CO_2, splitting water and producing H_2O_2, etc.

Carbon dioxide emissions from the massive burning of fossil fuels will cause the greenhouse effect. Photocatalysis can reduce CO_2 to other organic carbon materials [39], such as CO_2/CO (-0.11 V), CO_2/CH_4 (-0.244 V), CO_2/CH_3OH (-0.32 V), etc. It is a method of killing two birds with one stone to complete energy conversion while eliminating air pollution. Although g-C_3N_4 has Lewis and Brønsted active sites with CO_2 adsorption potential, the edge N atom becomes the limitation of CO_2 adsorption. So Su et al. [115] prepared g-C_3N_4 with the surface amino transformed into diazanyl

and then coupled with SnO_2, showing excellent performance of photocatalytic reduction of CO_2. The results of CO_2 adsorption/desorption showed that the increased specific surface area and the modified diazanyl were favorable for CO_2 adsorption. The results of DFT calculation revealed that the adsorption energy of CO_2 on g-C_3N_4 diazanyl (-0.17 V) was negative to the surface amino (-0.08 V), which theoretically explained the more stable adsorption of CO_2 on the diazo group. The process of CO_2 adsorption and reduction was analyzed by in-situ Fourier transform infrared spectroscopy. In Fig. 35, there were many carbonate peaks (monodentate carbonate (m-CO_3^{2-}), polydentate carbonate (p-CO_3^{2-}), bidentate carbonate (b-CO_3^{2-}), bicarbonate (HCO_3^-), carboxylate (CO_2^-), formate, etc.) under dark conditions, and a new peak belonging to HCOOH (1701 cm^{-1}) was generated after illumination for 1h. HCOOH is the intermediate product of CO_2 to CO conversion process, indicating that diazanyl modified SnO_2/g-C_3N_4 is more inclined to reduce CO_2 to CO. And its CO formation rate is as high as 21.5 μmol g^{-1} h^{-1}, which is 6 and 4.1 times higher than g-C_3N_4 and SnO_2/g-C_3N_4. In addition, Wajid Ali et al. [87] co-modified g-C_3N_4 with Ag and SnO_2 showed the CO_2 reduction activity is 10 times higher than that of pure g-C_3N_4, which can be attributed to the successful separation of electrons and holes and the extension of carrier lifetime. The transient photoluminescence spectra (TSPL) and the transient photoluminescence voltage (TPV) confirmed the excellent charge separation performance of Ag/SnO_2/g-C_3N_4, and the carrier lifetime is increased to 1.76 ms compared with g-C_3N_4 (0.53 ms).

The photocatalytic water splitting is known as artificial photosynthesis, which can transform light energy into chemical energy, as shown in Eq. (10) to (12). The photocatalytic splitting of water into hydrogen and oxygen is not spontaneous and requires the injection of additional energy, such as solar energy. Photogenerated electrons can reduce H^+ to release H_2, and photogenerated holes can oxidize H_2O to release O_2, but the oxygen evolution half reaction involves a relatively complex four-electron transfer process and becomes a rate-limiting step of water splitting [116].

$H_2O \rightarrow H_2 + 1/2\ O_2$ （$\triangle G^0$=237.13 kJ mol^{-1}） (10)

$2H_2O + 4h^+ \rightarrow O_2 + 4H^+$ (11)

$2H^+ + 2e^- \rightarrow H_2$ (12)

The SnO_2/g-C_3N_4 photocatalyst can be used for water splitting because it satisfies the redox potential of H^+/H_2 (0 V vs. NHE) and O_2/H_2O (1.23 V vs. NHE). It has been reported that SnO_2/g-C_3N_4 composite has the performance of photocatalytic splitting of water for hydrogen evolution [117]. And the main source of H_2 comes from the water molecules adsorbed on the surface of photocatalyst rather than the free H^+ in the solution [26]. Zang et al. [29] reported that SnO_2/g-C_3N_4 exhibited excellent photocatalytic performance for hydrogen evolution under visible light, and the hydrogen evolution rate (900 μmol g^{-1} h^{-1}) is much higher than that of pure g-C_3N_4. After loading Pt on SnO_2/g-C_3N_4, the photocatalytic hydrogen evolution rate can be further improved [118] , in which Pt can be replaced by Au or Ag [27]. Because it is very important to improve the utilization rate of photogenerated electrons for hydrogen evolution from water splitting. However, the capture process of conduction band electrons by oxygen vacancies competes with the direct hydrogen evolution of photogenerated electrons [51], but the captured electrons can be re-excited by infrared light with low energy to regain the activity of hydrogen evolution. In addition, Huang et al. [110] used the combination of g-C_3N_4 and TiO_2-SnO_2 sosoloid to form g-C_3N_4@TiO_2-SnO_2 with a hydrogen evolution rate of 220 μmol g^{-1} h^{-1}, due to its stronger charge separation performance and better reduction performance. Hydrogen evolution from water splitting by SnO_2/g-C_3N_4 composite has been reported, but there is no study on the simultaneous generation of O_2 and H_2 by SnO_2/g-C_3N_4 photocatalyst, which is a visible and worthwhile research opportunity.

Photocatalytic reduction of O_2 to H_2O_2 is also an important way of solar energy conversion and storage. The conversion from O_2 to H_2O_2 can be completed mainly through a two-step successive single electron reaction or a direct one-step two-electron reaction, as shown in Eq. (13) to (15). Obviously, dissolved oxygen plays a dominant

role in the photocatalytic production of H_2O_2. Chu et al. [119] modified g-C_3N_4 with cyanide group and SnO_2 to improve the performance of photocatalytic production of H_2O_2. Among them, cyanide group can reduce the band gap of g-C_3N_4 by increasing the ordered binding of triazine unit, while SnO_2 can be used as the electron accepter and O_2 adsorption sites, which is conducive to promoting the process of H_2O_2 generation.

$$O_2 + e^- \rightarrow \bullet O_2^- \quad (13)$$

$$\bullet O_2^- + 2H^+ + e^- \rightarrow H_2O_2 \quad (14)$$

$$O_2 + 2e^- \rightarrow H_2O_2 \quad (15)$$

5. Conclusions and perspectives

SnO_2/g-C_3N_4 Heterojunction can effectively solve many problems of a single semiconductor. For example, SnO_2 semiconductor has a narrow light absorption range and only absorbs ultraviolet light. Although g-C_3N_4 semiconductor has visible light response, it has a serious disadvantage of photogenerated electron hole recombination. The heterojunction interface between SnO_2 and g-C_3N_4 can achieve the directional transfer of photogenerated electrons and holes and effectively reduce recombination. Therefore, SnO_2/g-C_3N_4 heterojunction is a visible-light-driven photocatalyst with excellent electron hole separation efficiency. It has broad application prospects in environmental remediation and energy conversion.

In this review, several synthesis methods of SnO_2/g-C_3N_4 heterojunction are introduced. The performance optimization strategies of SnO_2/g-C_3N_4, including morphology control, defect introduction and multiple structural optimization strategies, are reviewed. Finally, the possible mechanisms and current applications of SnO_2/g-C_3N_4 heterojunction are discussed. Although great achievements have been made in research, there are still some severe challenges in practical large-scale photocatalytic application.

Firstly, a green and simple synthesis method is necessary to obtain SnO_2/g-C_3N_4

heterojunction photocatalyst. Therefore, it is of great significance to explore sustainable synthetic pathways with the potential for large-scale industrial production. We believe that obtaining SnO_2/g-C_3N_4 composite directly from the raw materials in one step without relying on the pre-prepared g-C_3N_4 and SnO_2 is a more excellent method to simplify the synthesis process and reduce production costs. In addition, the heterojunction system needs to focus on the problem of small interface contact and weak bonding. In summary, a variety of in-situ synthesis methods may provide possible solutions.

Secondly, the mechanism of heteroatom doping and defect is not clear enough, especially the position of local energy level caused by oxygen vacancy in the band gap has not reached a consensus. This problem can be further studied and explained by combining experiment with theoretical calculation. Moreover, the research on SnO_2/g-C_3N_4 dual-defect system is still scarce, which may provide a new idea for future performance optimization.

Thirdly, there is no direct evidence of interface bonding and carrier transport in SnO_2/g-C_3N_4 heterojunction. More advanced detection methods and higher resolution technologies are needed to realize in-situ characterization to clearly explain the mechanism of photocatalytic reaction, so as to manually intervene controllable steps to optimize photocatalytic performance. In addition, it is worth noting that there is a lack of powerful means to detect the intermediate and final products of the photocatalytic reaction process.

Fourthly, the working life and recyclability of the SnO_2/g-C_3N_4 photocatalyst should not be ignored, because long-term stability and durability are necessary for large-scale practical applications. It must be mentioned that although the experimental research of SnO_2/g-C_3N_4 photocatalyst has made great progress, it still has a long way to go before practical application. Because the actual application environment is more demanding, for example, there may be the coexistence of multiple complex pollutants in pollutant removal. And various influencing factors should be considered

comprehensively, including cost, effectiveness, durability, etc. In a word, we should continue to be committed to solving the above problems, so that theoretical research can be transformed into practical applications to achieve greater value in the future.

Acknowledgments

This work was financially supported by National Natural Science Foundation of China (No. 52172105), the Hebei Province Department of Higher Education Science and Technology Plan of Young Talents (No. BJ2018004) and S&T Program of Hebei Province (No. 20311001D)

References

[1] W. Zhong, W. Tu, S. Feng, A. Xu, Photocatalytic H_2 evolution on CdS nanoparticles by loading FeSe nanorods as co-catalyst under visible light irradiation, Journal of Alloys and Compounds, 772 (2019) 669-674.

[2] H. Yan, H. Yang, TiO_2−g-C_3N_4 composite materials for photocatalytic H_2 evolution under visible light irradiation, Journal of Alloys and Compounds, 509 (2011) L26-L29.

[3] X. Lin, M. Sun, B. Gao, W. Ding, Z. Zhang, S. Anandan, A. Umar, Hydrothermally regulating phase composition of TiO_2 nanocrystals toward high photocatalytic activity, Journal of Alloys and Compounds, 850 (2021) 156653.

[4] X. Li, J. Xiong, X. Gao, J. Huang, Z. Feng, Z. Chen, Y. Zhu, Recent advances in 3D g-C_3N_4 composite photocatalysts for photocatalytic water splitting, degradation of pollutants and CO_2 reduction, Journal of Alloys and Compounds, 802 (2019) 196-209.

[5] Z. Zhang, C. Gao, Z. Wu, W. Han, Y. Wang, W. Fu, X. Li, E. Xie, Toward efficient photoelectrochemical water-splitting by using screw-like SnO_2 nanostructures as photoanode after being decorated with CdS quantum dots, Nano Energy, 19 (2016) 318-327.

[6] L. Zhang, C. Niu, C. Liang, X. Wen, D. Huang, H. Guo, X. Zhao, G. Zeng, One-step in situ synthesis of CdS/SnO_2 heterostructure with excellent photocatalytic performance for Cr(VI) reduction and tetracycline degradation, Chemical Engineering Journal, 352 (2018) 863-875.

[7] Z. Zhang, C. Gao, Z. Wu, W. Han, Y. Wang, W. Fu, X. Li, E. Xie, Toward efficient photoelectrochemical water-splitting by using screw-like SnO_2 nanostructures as photoanode after being decorated with CdS quantum dots, Nano Energy, 19 (2016) 318-327.

[8] Z. Zhang, C. Shao, X. Li, L. Zhang, H. Xue, C. Wang, Y. Liu, Electrospun Nanofibers of ZnO-SnO_2 Heterojunction with High Photocatalytic Activity, The Journal of Physical Chemistry C, 114 (2010) 7920-7925.

[9] L. Zhu, M. Hong, G. Wei Ho, Hierarchical Assembly of SnO_2/ZnO Nanostructures for Enhanced Photocatalytic Performance, Scientific Reports, 5 (2015).

[10] L. Zheng, Y. Zheng, C. Chen, Y. Zhan, X. Lin, Q. Zheng, K. Wei, J. Zhu, Network Structured SnO_2/ZnO Heterojunction Nanocatalyst with High Photocatalytic Activity, Inorganic Chemistry, 48 (2009) 1819-1825.

[11] Y.C. Zhang, L. Yao, G. Zhang, D.D. Dionysiou, J. Li, X. Du, One-step hydrothermal synthesis of high-performance visible-light-driven SnS_2/SnO_2 nanoheterojunction photocatalyst for the reduction of aqueous Cr(VI), Applied Catalysis B: Environmental, 144 (2014) 730-738.

[12] X. Zhang, P. Zhang, L. Wang, H. Gao, J. Zhao, C. Liang, J. Hu, G. Shao, Template-oriented synthesis of monodispersed SnS_2@SnO_2 hetero-nanoflowers for Cr(VI) photoreduction, Applied Catalysis B: Environmental, 192 (2016) 17-25.

[13] J. Mu, F. Teng, H. Miao, Y. Wang, X. Hu, In-situ oxidation fabrication of 0D/2D SnO_2/SnS_2 novel Step-scheme heterojunctions with enhanced photoelectrochemical activity for water splitting, Applied Surface Science, 501 (2020) 143974.

[14] S. Zhou, R. Tang, L. Zhang, L. Yin, Au Nanoparticles coupled Three-dimensional Macroporous $BiVO_4$/SnO_2 Inverse Opal Heterostructure For Efficient Photoelectrochemical Water Splitting, Electrochimica Acta, 248 (2017) 593-602.

[15] J. Yin, S. Huang, Z. Jian, Z. Wang, Y. Zhang, Fabrication of heterojunction $SnO_2/BiVO_4$ composites having enhanced visible light photocatalystic activity, Materials Science in Semiconductor Processing, 34 (2015) 198-204.

[16] J. Yang, N. Sun, Z. Zhang, J. Bian, Y. Qu, Z. Li, M. Xie, W. Han, L. Jing, Ultrafine SnO_2/010 Facet-Exposed $BiVO_4$ Nanocomposites as Efficient Photoanodes for Controllable Conversion of 2,4-Dichlorophenol via a Preferential Dechlorination Path, ACS Applied Materials & Interfaces, 12 (2020) 28264-28272.

[17] B. Zhang, W. Fu, X. Meng, A. Ruan, P. Su, H. Yang, Enhanced ethanol sensing properties based on spherical-coral-like SnO_2 nanorods decorated with α-Fe_2O_3 nanocrystallites, Sensors and Actuators B: Chemical, 261 (2018) 505-514.

[18] C. Zhu, Y. Li, Q. Su, B. Lu, J. Pan, J. Zhang, E. Xie, W. Lan, Electrospinning direct preparation of SnO_2/Fe_2O_3 heterojunction nanotubes as an efficient visible-light photocatalyst, Journal of Alloys and Compounds, 575 (2013) 333-338.

[19] L. Gomathi Devi, R. Shyamala, Photocatalytic activity of SnO_2−α-Fe_2O_3 composite mixtures: exploration of number of active sites, turnover number and turnover frequency, Materials chemistry frontiers, 2 (2018) 796-806.

[20] H. Shen, X. Zhao, L. Duan, R. Liu, H. Li, Enhanced visible light photocatalytic activity in SnO_2@g-C_3N_4 core-shell structures, Materials Science and Engineering: B, 218 (2017) 23-30.

[21] Z.Q. Li, Y.L. Yin, X.D. Liu, L.Y. Li, H. Liu, Q.G. Song, Electronic structure and optical properties of Sb-doped SnO_2, Journal of Applied Physics, 106 (2009) 083701.

[22] A. Seko, A. Togo, F. Oba, I. Tanaka, Structure and Stability of a Homologous Series of Tin Oxides, Physical review letters, 100 (2008) 045702-045702.

[23] X. Wang, X. Chen, A. Thomas, X. Fu, M. Antonietti, Metal-Containing Carbon Nitride Compounds: A New Functional Organic-Metal Hybrid Material, Advanced Materials, 21 (2009) 1609-1612.

[24] J. Liu, Effect of phosphorus doping on electronic structure and photocatalytic performance of g-C_3N_4: Insights from hybrid density functional calculation, Journal of Alloys and Compounds, 672 (2016) 271-276.

[25] H. Xu, Y. Xu, H. Li, J. Xia, J. Xiong, S. Yin, C. Huang, H. Wan, Synthesis, characterization and photocatalytic property of $AgBr/BiPO_4$ heterojunction photocatalyst, Dalton transactions: an international journal of inorganic chemistry, 41 (2012) 3387-3394.

[26] X. Zhang, X. Zhang, J. Li, J. Sun, J. Bian, J. Wang, Y. Qu, R. Yan, C. Qin, L. Jing, Exceptional visible-light activities of g-C_3N_4 nanosheets dependent on the unexpected synergistic effects of prolonging charge lifetime and catalyzing H_2 evolution with H_2O, Applied Catalysis B: Environmental, 237 (2018) 50-58.

[27] A. Zada, M. Humayun, F. Raziq, X. Zhang, Y. Qu, L. Bai, C. Qin, L. Jing, H. Fu, Exceptional Visible-Light-Driven Cocatalyst-Free Photocatalytic Activity of g-C_3N_4 by Well Designed Nanocomposites with Plasmonic Au and SnO_2, Advanced Energy Materials, 6 (2016) 1601190.

[28] R. Yin, Q. Luo, D. Wang, H. Sun, Y. Li, X. Li, J. An, SnO_2/g-C_3N_4 photocatalyst with enhanced visible-light photocatalytic activity, Journal of Materials Science, 49 (2014) 6067-6073.

[29] Y. Zang, L. Li, X. Li, R. Lin, G. Li, Synergistic collaboration of g-C_3N_4/SnO_2 composites for enhanced visible-light photocatalytic activity, Chemical Engineering Journal, 246 (2014) 277-286.

[30] J. Zhang, L. Li, T. Yan, G. Li, Selective Pt Deposition onto the Face (110) of TiO_2 Assembled Microspheres That Substantially Enhances the Photocatalytic Properties, The Journal of Physical

Chemistry C, 115 (2011) 13820-13828.

[31] M. Zhao, L. Li, J. Zheng, L. Yang, G. Li, Is $BiPO_4$ a better luminescent host? Case study on doping and annealing effects, Inorg Chem, 52 (2013) 807-15.

[32] A. Zada, M. Khan, M.N. Qureshi, S.Y. Liu, R. Wang, Accelerating Photocatalytic Hydrogen Production and Pollutant Degradation by Functionalizing g-C_3N_4 With SnO_2, Front Chem, 7 (2019) 941.

[33] K. Zhu, Y. Lv, J. Liu, W. Wang, C. Wang, S. Li, P. Wang, M. Zhang, A. Meng, Z. Li, Facile fabrication of g-C_3N_4/SnO_2 composites and ball milling treatment for enhanced photocatalytic performance, Journal of Alloys and Compounds, 802 (2019) 13-18.

[34] A. Mohammad, M.E. Khan, M.R. Karim, M.H. Cho, Synergistically effective and highly visible light responsive SnO_2-g-C_3N_4 nanostructures for improved photocatalytic and photoelectrochemical performance, Applied Surface Science, 495 (2019) 143432.

[35] M.U. Yousaf, E. Pervaiz, S. Minallah, M.J. Afzal, L. Honghong, M. Yang, Tin oxide quantum dots decorated graphitic carbon nitride for enhanced removal of organic components from water: Green process, Results in Physics, 14 (2019) 102455.

[36] H. Ji, Y. Fan, J. Yan, Y. Xu, X. She, J. Gu, T. Fei, H. Xu, H. Li, Construction of SnO_2/graphene-like g-C_3N_4 with enhanced visible light photocatalytic activity, RSC Advances, 7 (2017) 36101-36111.

[37] C. Wang, Y. Zhou, M. Ge, X. Xu, Z. Zhang, J.Z. Jiang, Large-Scale Synthesis of SnO_2 Nanosheets with High Lithium Storage Capacity, Journal of the American Chemical Society, 132 (2010) 46-47.

[38] X. Wang, P. Ren, Flower-like SnO_2/g-C_3N_4 heterojunctions: The face-to-face contact interface and improved photocatalytic properties, Advanced Powder Technology, 29 (2018) 1153-1157.

[39] Y. He, L. Zhang, M. Fan, X. Wang, M.L. Walbridge, Q. Nong, Y. Wu, L. Zhao, Z-scheme SnO_{2-x}/g-C_3N_4 composite as an efficient photocatalyst for dye degradation and photocatalytic CO_2 reduction, Solar Energy Materials and Solar Cells, 137 (2015) 175-184.

[40] Y.H.A.R. Qi Li, One-step synthesis of SnO_2 nanoparticles-loaded graphitic carbon nitride and their application in thermal decomposition of ammonium perchlorate, The Royal Society of Chemistry and the Centre National de la Recherche Scientifique, 39 (2015) 8703.

[41] C. Fettkenhauer, G. Clavel, K. Kailasam, M. Antonietti, D. Dontsova, Facile synthesis of new, highly efficient SnO_2/carbon nitride composite photocatalysts for the hydrogen evolution reaction, Green Chemistry, 17 (2015) 3350-3361.

[42] L. Peng, R. Zheng, D. Feng, H. Yu, X. Dong, Synthesis of eco-friendly porous g-C_3N_4/SiO_2/SnO_2 composite with excellent visible-light responsive photocatalysis, Arabian Journal of Chemistry, 13 (2020) 4275-4285.

[43] C. Yu, H. He, X. Liu, J. Zeng, Z. Liu, Novel SiO_2 nanoparticle-decorated BiOCl nanosheets exhibiting high photocatalytic performances for the removal of organic pollutants, Chinese journal of catalysis, 40 (2019) 1212-1221.

[44] Y. Chen, W. Li, D. Jiang, K. Men, Z. Li, L. Li, S. Sun, J. Li, Z. Huang, L. Wang, Facile synthesis of bimodal macroporous g-C_3N_4/SnO_2 nanohybrids with enhanced photocatalytic activity, Science Bulletin, 64 (2019) 44-53.

[45] A. Seza, F. Soleimani, N. Naseri, M. Soltaninejad, S.M. Montazeri, S.K. Sadrnezhaad, M.R. Mohammadi, H.A. Moghadam, M. Forouzandeh, M.H. Amin, Novel microwave-assisted synthesis of porous g-C_3N_4/SnO_2 nanocomposite for solar water-splitting, Applied Surface Science, 440 (2018) 153-161.

[46] K. Li, X. Zeng, S. Gao, L. Ma, Q. Wang, H. Xu, Z. Wang, B. Huang, Y. Dai, J. Lu, Ultrasonic-

assisted pyrolyzation fabrication of reduced SnO_{2-x}/g-C_3N_4 heterojunctions: Enhance photoelectrochemical and photocatalytic activity under visible LED light irradiation, Nano Research, 9 (2016) 1969-1982.

[47] P. Praus, L. Svoboda, R. Dvorský, M. Reli, Nanocomposites of SnO_2 and g-C_3N_4: Preparation, characterization and photocatalysis under visible LED irradiation, Ceramics International, 44 (2018) 3837-3846.

[48] A. Akhundi, A. Habibi-Yangjeh, A simple large-scale method for preparation of g-C_3N_4/SnO_2 nanocomposite as visible-light-driven photocatalyst for degradation of an organic pollutant, Materials Express, 5 (2015) 309-318.

[49] D. Chen, S. Huang, R. Huang, Q. Zhang, T. Le, E. Cheng, Z. Hu, Z. Chen, Highlights on advances in SnO_2 quantum dots: insights into synthesis strategies, modifications and applications, Materials research letters, 6 (2018) 462-488.

[50] J. Du, R. Zhao, Y. Xie, J. Li, Size-controlled synthesis of SnO_2 quantum dots and their gas-sensing performance, Applied Surface Science, 346 (2015) 256-262.

[51] X. Chen, L. Li, Y. Zhang, Y. Xu, G. Li, Re-excitation of localized electrons in SnO_2 quantum dots for enhanced water photolysis activity, RSC Advances, 6 (2016) 83848-83855.

[52] C. Burda, X. Chen, R. Narayanan, M.A. El-Sayed, Chemistry and Properties of Nanocrystals of Different Shapes, Chemical Reviews, 105 (2005) 1025-1102.

[53] J. Liu, Q. Zhang, X. Tian, Y. Hong, Y. Nie, N. Su, G. Jin, Z. Zhai, C. Fu, Highly efficient photocatalytic degradation of oil pollutants by oxygen deficient SnO_2 quantum dots for water remediation, Chemical Engineering Journal, 404 (2021) 127146.

[54] B. Babu, M. Cho, C. Byon, J. Shim, Sunlight-driven photocatalytic activity of SnO_2 QDs-g-C3N4 nanolayers, Materials Letters, 212 (2018) 327-331.

[55] P. Zhang, L. Wang, X. Zhang, J. Hu, G. Shao, Three-dimensional Porous Networks of Ultra-long Electrospun SnO_2 Nanotubes with High Photocatalytic Performance, Nano-Micro Letters, 7 (2015) 86-95.

[56] H. Hou, X. Zhang, Rational design of 1D/2D heterostructured photocatalyst for energy and environmental applications, Chemical Engineering Journal, 395 (2020) 125030.

[57] J. Wu, Y. Zhang, J. Zhou, K. Wang, Y. Zheng, X. Tao, Uniformly assembling n-type metal oxide nanostructures (TiO_2 nanoparticles and SnO_2 nanowires) onto P doped g-C_3N_4 nanosheets for efficient photocatalytic water splitting, Applied Catalysis B: Environmental, 278 (2020) 119301.

[58] M.Z. Qin, W.X. Fu, H. Guo, C.G. Niu, D.W. Huang, C. Liang, Y.Y. Yang, H.Y. Liu, N. Tang, Q.Q. Fan, 2D/2D Heterojunction systems for the removal of organic pollutants: A review, Adv Colloid Interface Sci, 297 (2021) 102540.

[59] H. Hou, X. Zeng, X. Zhang, 2D/2D heterostructured photocatalyst: Rational design for energy and environmental applications, Science China Materials, 63 (2020) 2119-2152.

[60] R. Ghosh Chaudhuri, S. Paria, Core/Shell Nanoparticles: Classes, Properties, Synthesis Mechanisms, Characterization, and Applications, Chemical Reviews, 112 (2012) 2373-2433.

[61] R. Dvorský, J. Trojková, P. Praus, J. Luňáček, Analysis of mechanisms of composite particles modification in liquid dispersions, Materials Research Bulletin, 48 (2013) 2286-2288.

[62] L. Yang, J. Huang, L. Shi, L. Cao, H. Liu, Y. Liu, Y. Li, H. Song, Y. Jie, J. Ye, Sb doped SnO_2-decorated porous g-C_3N_4 nanosheet heterostructures with enhanced photocatalytic activities under visible light irradiation, Applied Catalysis B: Environmental, 221 (2018) 670-680.

[63] W. Gao, Y. Zhao, Z. Mao, D. Bi, J. Chen, D. Wang, Enhanced visible light photocatalytic activity

for g-C_3N_4/SnO_2:Sb composites induced by Sb doping, Journal of Materials Science, 53 (2018) 9473-9485.

[64] L. Villamagua, F. Maldonado, D. Castillo, M. Carini, Doping SnO_2 crystal with increasing concentrations of Zn and Sb atoms: a quantum chemical analysis, Physica scripta, 93 (2018) 95801.

[65] M. Jourshabani, Z. Shariatinia, A. Badiei, In situ fabrication of SnO_2/S-doped g-C_3N_4 nanocomposites and improved visible light driven photodegradation of methylene blue, Journal of Molecular Liquids, 248 (2017) 688-702.

[66] F. Raziq, Y. Qu, M. Humayun, A. Zada, H. Yu, L. Jing, Synthesis of SnO_2/B-P codoped g-C_3N_4 nanocomposites as efficient cocatalyst-free visible-light photocatalysts for CO2 conversion and pollutant degradation, Applied Catalysis B: Environmental, 201 (2017) 486-494.

[67] X. Ma, Y. Lv, J. Xu, Y. Liu, R. Zhang, Y. Zhu, A Strategy of Enhancing the Photoactivity of g-C_3N_4 via Doping of Nonmetal Elements: A First-Principles Study, The Journal of Physical Chemistry C, 116 (2012) 23485-23493.

[68] L. Zhang, B. Han, P. Cheng, Y.H. Hu, In-situ FTIR-DRS investigation on shallow trap state of Cu-doped TiO_2 photocatalyst, Catalysis today, 341 (2020) 21-25.

[69] F.S. Al Mashary, J.F. Felix, S.O. Ferreira, D. de Souza, Y.G. Gobato, J. Chauhan, N. Alexeeva, M. Henini, A.M. Albadri, A.Y. Alyamani, Investigation of the structural, optical and electrical properties of indium-doped TiO_2 thin films grown by Pulsed Laser Deposition technique on low and high index GaAs planes, Materials Science and Engineering: B, 259 (2020) 114578.

[70] H. He, Z. Xie, Q. Li, H. Niu, On the possibility of p-type doping of SnO_2 with Mg: A first-principles study, Computational Materials Science, 101 (2015) 62-65.

[71] Du Juan, J. ZhenGuo, The effect of III-family element doping on electronic structures and electrical characteristics of SnO_2, ACTA PHYSICA SINICA, 56 (2007) 2388-2392.

[72] S. Li, L. Zhang, T. Jiang, L. Chen, Y. Lin, D. Wang, T. Xie, Construction of Shallow Surface States through Light Ni Doping for High-Efficiency Photocatalytic Hydrogen Production of CdS Nanocrystals, Chemistry - A European Journal, 20 (2014) 311-316.

[73] F. Yu, C. Wang, Y. Li, H. Ma, R. Wang, Y. Liu, N. Suzuki, C. Terashima, B. Ohtani, T. Ochiai, A. Fujishima, X. Zhang, Enhanced Solar Photothermal Catalysis over Solution Plasma Activated TiO_2, Advanced Science, 7 (2020) 2000204.

[74] J. Robertson, P.W. Peacock, Doping and hydrogen in wide gap oxides, Thin Solid Films, 445 (2003) 155-160.

[75] Ç.K.A.A. Zunger, Origins of Coexistence of Conductivity and Transparency in SnO_2, PHYSICAL REVIEW LETTERS, (2002).

[76] S. Anuchai, S. Phanichphant, D. Tantraviwat, P. Pluengphon, T. Bovornratanaraks, B. Inceesungvorn, Low temperature preparation of oxygen-deficient tin dioxide nanocrystals and a role of oxygen vacancy in photocatalytic activity improvement, Journal of Colloid and Interface Science, 512 (2018) 105-114.

[77] C. Fan, Y. Peng, Q. Zhu, L. Lin, R. Wang, A. Xu, Synproportionation Reaction for the Fabrication of Sn^{2+} Self-Doped SnO_{2-x} Nanocrystals with Tunable Band Structure and Highly Efficient Visible Light Photocatalytic Activity, The Journal of Physical Chemistry C, 117 (2013) 24157-24166.

[78] M. Sun, Y. Su, C. Du, Q. Zhao, Z. Liu, Self-doping for visible light photocatalytic purposes: construction of SiO_2/SnO_2/SnO_2:Sn^{2+} nanostructures with tunable optical and photocatalytic performance, RSC Advances, 4 (2014) 30820.

[79] L. Huang, F. Zhang, Y. Li, P. Ding, P. Li, H. Xu, H. Li, Partial Oxidation of Sn^{2+} Induced Oxygen

Vacancy Overspread on the Surface of SnO_{2-x}/g-C_3N_4 Composites for Enhanced LED-Light-Driven Photoactivity, Journal of Inorganic and Organometallic Polymers and Materials, 29 (2019) 765-775.

[80] Y. Duan, W. Yang, W. Zheng, G. He, M. Chen, M. Tian, Solar Hydrogen Production from Cost Effective Stannic Oxide Under Visible Light Irradiation, Nanoscale Research Letters, 14 (2019).

[81] Y. Wang, D. Meng, X. Zhao, Visible-light-driven H_2O_2 production from O_2 reduction with nitrogen vacancy-rich and porous graphitic carbon nitride, Applied Catalysis B: Environmental, 273 (2020) 119064.

[82] H. Chi, J. Liu, X. Zhang, X. Xue, D. Zhang, X. Lin, P. Huang, L. Sun, J. Xiong, P. Cai, J. Zhang, Synergetic defects boost charge separation in CN for enhanced photocatalytic water splitting, Journal of materials chemistry. C, Materials for optical and electronic devices, 8 (2020) 9366-9372.

[83] L. Shi, L. Yang, W. Zhou, Y. Liu, L. Yin, X. Hai, H. Song, J. Ye, Photoassisted Construction of Holey Defective g-C_3N_4 Photocatalysts for Efficient Visible-Light-Driven H_2O_2 Production, Small, 14 (2018) 1703142.

[84] J. Xu, Z. Wang, Y. Zhu, Highly efficient visible photocatalytic disinfection and degradation performances of microtubular nanoporous g-C_3N_4 via hierarchical construction and defects engineering, Journal of Materials Science & Technology, 49 (2020) 133-143.

[85] H. Gao, R. Cao, X. Xu, S. Zhang, H. Yongshun, H. Yang, X. Deng, J. Li, Construction of dual defect mediated Z-scheme photocatalysts for enhanced photocatalytic hydrogen evolution, Applied Catalysis B: Environmental, 245 (2019) 399-409.

[86] Z. Fang, X. Huang, Y. Wang, W. Feng, Y. Zhang, S. Weng, X. Fu, P. Liu, Dual-defective strategy directing in situ assembly for effective interfacial contacts in MoS_2 cocatalyst/In_2S_3 light harvester layered photocatalysts, Journal of Materials Chemistry A, 4 (2016) 13980-13988.

[87] W. Ali, X. Zhang, X. Zhang, S. Ali, L. Zhao, S. Shaheen, L. Jing, Improved visible-light activities of g-C_3N_4 nanosheets by co-modifying nano-sized SnO_2 and Ag for CO_2 reduction and 2,4-dichlorophenol degradation, Materials Research Bulletin, 122 (2020) 110676.

[88] A. Mohammad, M.R. Karim, M.E. Khan, M.M. Khan, M.H. Cho, Biofilm-Assisted Fabrication of Ag@SnO_2-g-C_3N_4 Nanostructures for Visible Light-Induced Photocatalysis and Photoelectrochemical Performance, The Journal of Physical Chemistry C, 123 (2019) 20936-20948.

[89] B. Babu, R. Koutavarapu, J. Shim, K. Yoo, Enhanced visible-light-driven photoelectrochemical and photocatalytic performance of Au-SnO_2 quantum dot-anchored g-C_3N_4 nanosheets, Separation and Purification Technology, 240 (2020) 116652.

[90] Z. Zhang, J.T. Yates, Band Bending in Semiconductors: Chemical and Physical Consequences at Surfaces and Interfaces, Chemical Reviews, 112 (2012) 5520-5551.

[91] Y. Yang, X. Yang, D. Leng, S. Wang, W. Zhang, Fabrication of g-C_3N_4/SnS_2/SnO_2 nanocomposites for promoting photocatalytic reduction of aqueous Cr(VI) under visible light, Chemical Engineering Journal, 335 (2018) 491-500.

[92] F. Yuan, Z. Sun, C. Li, Y. Tan, X. Zhang, S. Zheng, Multi-component design and in-situ synthesis of visible-light-driven SnO_2/g-C_3N_4/diatomite composite for high-efficient photoreduction of Cr(VI) with the aid of citric acid, Journal of Hazardous Materials, 396 (2020) 122694.

[93] M. Faraji, N. Mohaghegh, A. Abedini, Ternary composite of TiO_2 nanotubes/Ti plates modified by g-C_3N_4 and SnO_2 with enhanced photocatalytic activity for enhancing antibacterial and photocatalytic activity, Journal of Photochemistry and Photobiology B: Biology, 178 (2018) 124-132.

[94] S.V.P. Vattikuti, P.A.K. Reddy, J. Shim, C. Byon, Visible-Light-Driven Photocatalytic Activity of

SnO_2−ZnO Quantum Dots Anchored on g-C_3N_4 Nanosheets for Photocatalytic Pollutant Degradation and H_2 Production, ACS Omega, 3 (2018) 7587-7602.

[95] M. Danish, M. Muneer, Novel ZnSQDs-SnO_2/g-C_3N_4 nanocomposite with enhanced photocatalytic performance for the degradation of different organic pollutants in aqueous suspension under visible light, Journal of Physics and Chemistry of Solids, 149 (2021) 109785.

[96] C. Sun, J. Yang, Y. Zhu, M. Xu, Y. Cui, L. Liu, W. Ren, H. Zhao, B. Liang, Synthesis of 0D SnO_2 nanoparticles/2D g-C_3N_4 nanosheets heterojunction: improved charge transfer and separation for visible-light photocatalytic performance, Journal of Alloys and Compounds, (2021) 159561.

[97] M. Nguyen-Dinh, T.S. Bui, P. Bansal, M. Jourshabani, B. Lee, Photocatalytic and photo-electrochemical behavior of novel SnO_2-modified-g-C_3N_4 for complete elimination of tetracycline under visible-light irradiation: Slurry and fixed-bed approach, Separation and Purification Technology, 267 (2021) 118607.

[98] S. Asaithambi, P. Sakthivel, M. Karuppaiah, R. Yuvakkumar, D. Velauthapillai, T. Ahamad, M.A.M. Khan, M.K.A. Mohammed, N. Vijayaprabhu, G. Ravi, The bifunctional performance analysis of synthesized Ce doped SnO_2/g-C_3N_4 composites for asymmetric supercapacitor and visible light photocatalytic applications, Journal of Alloys and Compounds, 866 (2021) 158807.

[99] T. Zhang, F. Chang, Y. Qi, X. Zhang, J. Yang, X. Liu, S. Li, A facile one-pot and alkali-free synthetic procedure for binary SnO_2/g-C_3N_4 composites with enhanced photocatalytic behavior, Materials Science in Semiconductor Processing, 115 (2020) 105112.

[100] J. Low, J. Yu, M. Jaroniec, S. Wageh, A.A. Al-Ghamdi, Heterojunction Photocatalysts, Advanced Materials, 29 (2017) 1601694.

[101] Q. Wang, J. Tian, L. Wei, Y. Liu, C. Yang, Z-scheme heterostructure of Fe-doped SnO_2 decorated layered g-C_3N_4 with enhanced photocatalytic activity under simulated solar light irradiation, Optical Materials, 101 (2020) 109769.

[102] Z. Bao, M. Xing, Y. Zhou, J. Lv, D. Lei, Y. Zhang, J. Cai, J. Wang, Z. Sun, W. Chen, X. Gan, X. Yang, Q. Han, M. Zhang, J. Dai, Y. Wu, Z−Scheme Flower−Like SnO_2/g-C_3N_4 Composite with Sn^{2+} Active Center for Enhanced Visible−Light Photocatalytic Activity, Advanced Sustainable Systems, 5 (2021) 2100087.

[103] Q. Xu, L. Zhang, B. Cheng, J. Fan, J. Yu, S-Scheme Heterojunction Photocatalyst, Chem, 6 (2020) 1543-1559.

[104] D. Bui, T. Nguyen, T.T. Le Vo, T.M. Cao, S. You, V.V. Pham, SnO_{2-x} Nanoparticles Decorated on Graphitic Carbon Nitride as S-Scheme Photocatalysts for Activation of Peroxymonosulfate, ACS Applied Nano Materials, 4 (2021) 9333-9343.

[105] V. Van Pham, D. Mai, D. Bui, T. Van Man, B. Zhu, L. Zhang, J. Sangkaworn, J. Tantirungrotechai, V. Reutrakul, T.M. Cao, Emerging 2D/0D g-C_3N_4/SnO_2 S-scheme photocatalyst: New generation architectural structure of heterojunctions toward visible-light-driven NO degradation, Environmental Pollution, 286 (2021) 117510.

[106] J. Singh, P. Kumari, S. Basu, Degradation of toxic industrial dyes using SnO_2/g-C_3N_4 nanocomposites: Role of mass ratio on photocatalytic activity, Journal of Photochemistry and Photobiology A: Chemistry, 371 (2019) 136-143.

[107] D. Li, J. Huang, R. Li, P. Chen, D. Chen, M. Cai, H. Liu, Y. Feng, W. Lv, G. Liu, Synthesis of a carbon dots modified g-C_3N_4/SnO_2 Z-scheme photocatalyst with superior photocatalytic activity for PPCPs degradation under visible light irradiation, Journal of Hazardous Materials, 401 (2021) 123257.

[108] S. Khan, C. Wan, J. Chen, I. Khan, M. Luo, C. Wang, Eriobotrya japonica assisted green synthesis

of g-C_3N_4 nanocomposites and its exceptional photoactivities for doxycycline and rhodamine B degradation with mechanism insight, Journal of the Chinese Chemical Society, 68 (2021) 2093-2102.
[109] S. Vignesh, G. Palanisamy, M. Srinivasan, N. Elavarasan, K. Bhuvaneswari, G. Venkatesh, T. Pazhanivel, P. Ramasamy, M.A. Manthrammel, M. Shkir, Fabricating SnO_2 and Cu_2O anchored on g-C_3N_4 nanocomposites for superior photocatalytic various organic pollutants degradation under simulated sunlight exposure, Diamond and Related Materials, 120 (2021) 108606.
[110] M. Huang, J. Li, Y. Huang, X. Zhou, Z. Qin, Z. Tong, M. Fan, B. Li, L. Dong, Construction of g-C3N4 based heterojunction photocatalyst by coupling TiO_2-SnO_2 solid solution for efficient multipurpose photocatalysis, Journal of Alloys and Compounds, 864 (2021) 158132.
[111] Y. Wang, Y. Su, W. Fang, Y. Zhang, X. Li, G. Zhang, W. Sun, SnO_2/SnS_2 nanocomposite anchored on nitrogen-doped RGO for improved photocatalytic reduction of aqueous Cr(VI), Powder Technology, 363 (2020) 337-348.
[112] X. Chen, Q. Wang, J. Tian, Y. Liu, Y. Wang, C. Yang, A study on the photocatalytic sterilization performance and mechanism of Fe-SnO_2/g-C_3N_4 heterojunction materials, New journal of chemistry, 44 (2020) 9456-9465.
[113] Y. Zou, Y. Xie, S. Yu, L. Chen, W. Cui, F. Dong, Y. Zhou, SnO_2 quantum dots anchored on g-C_3N_4 for enhanced visible-light photocatalytic removal of NO and toxic NO_2 inhibition, Applied Surface Science, 496 (2019) 143630.
[114] P. Van Viet, H. Nguyen, H. Tran, D. Bui, L.V. Hai, M. Pham, S. You, C.M. Thi, Constructing g-C_3N_4/SnO_2 S-scheme heterojunctions for efficient photocatalytic NO removal and low NO_2 generation, Journal of Science: Advanced Materials and Devices, 6 (2021) 551-559.
[115] F. Su, Y. Chen, R. Wang, S. Zhang, K. Liu, Y. Zhang, W. Zhao, C. Ding, H. Xie, L. Ye, Diazanyl and SnO_2 bi-activated g-C_3N_4 for enhanced photocatalytic CO_2 reduction, Sustainable Energy & Fuels, 5 (2021) 1034-1043.
[116] A.K.A.Y. Miseki, Heterogeneous photocatalyst materials for water splitting, Chemical Society Reviews, 38 (2009) 253-278.
[117] H. Wu, S. Yu, Y. Wang, J. Han, L. Wang, N. Song, H. Dong, C. Li, A facile one-step strategy to construct 0D/2D SnO_2/g-C_3N_4 heterojunction photocatalyst for high-efficiency hydrogen production performance from water splitting, International Journal of Hydrogen Energy, 45 (2020) 30142-30152.
[118] X. Wang, M. Xue, X. Li, L. Qin, S. Kang, Boosting the photocatalytic H_2 production performance and stability of C_3N_4 nanosheets via the synergistic effect between SnO_2 nanoparticles and Pt nanoclusters, Inorganic Chemistry Communications, 133 (2021) 108976.
[119] C. Chu, W. Miao, Q. Li, D. Wang, Y. Liu, S. Mao, Highly efficient photocatalytic H_2O_2 production with cyano and SnO_2 co-modified g-C_3N_4, Chemical Engineering Journal, 428 (2022) 132531.
[120] X. Chen, B. Zhou, S. Yang, H. Wu, Y. Wu, L. Wu, J. Pan, X. Xiong, In situ construction of an SnO_2/g-C_3N_4 heterojunction for enhanced visible-light photocatalytic activity, RSC Advances, 5 (2015) 68953-68963.
[121] B. Tao, Z. Yan, In-situ synthesis of highly efficient visible light driven stannic oxide/graphitic carbon nitride heterostructured photocatalysts, Journal of Colloid and Interface Science, 480 (2016) 118-125.
[122] X. Han, J. Zhao, L. An, Z. Li, Y. Xin, One-step synthesis of oxygen vacancy-rich SnO_2 quantum dots with ultrahigh visible-light photocatalytic activity, Materials Research Bulletin, 118 (2019) 110486.

Figures

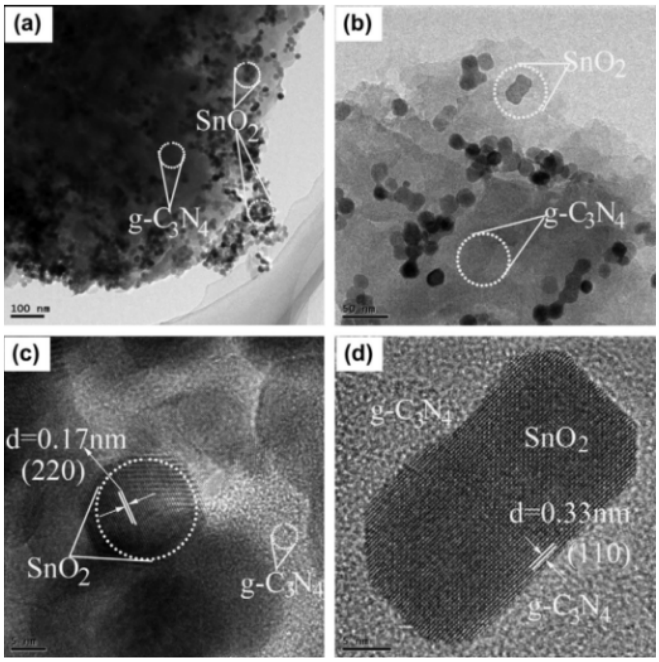

Fig. 1 TEM and HRTEM images of g-C_3N_4/SnO_2. [29]

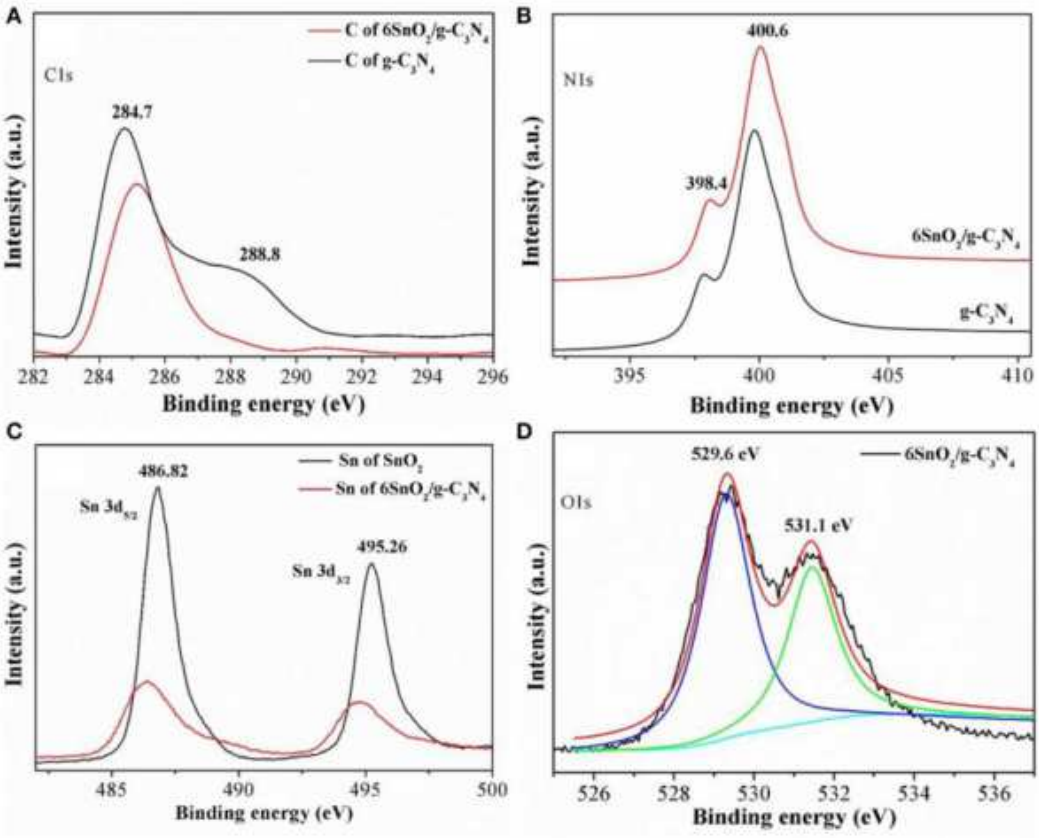

Fig. 2 X-ray photoelectron spectra of C 1s, N 1s, Sn 3d and O 1s of g-C_3N_4 and SnO_2. [32]

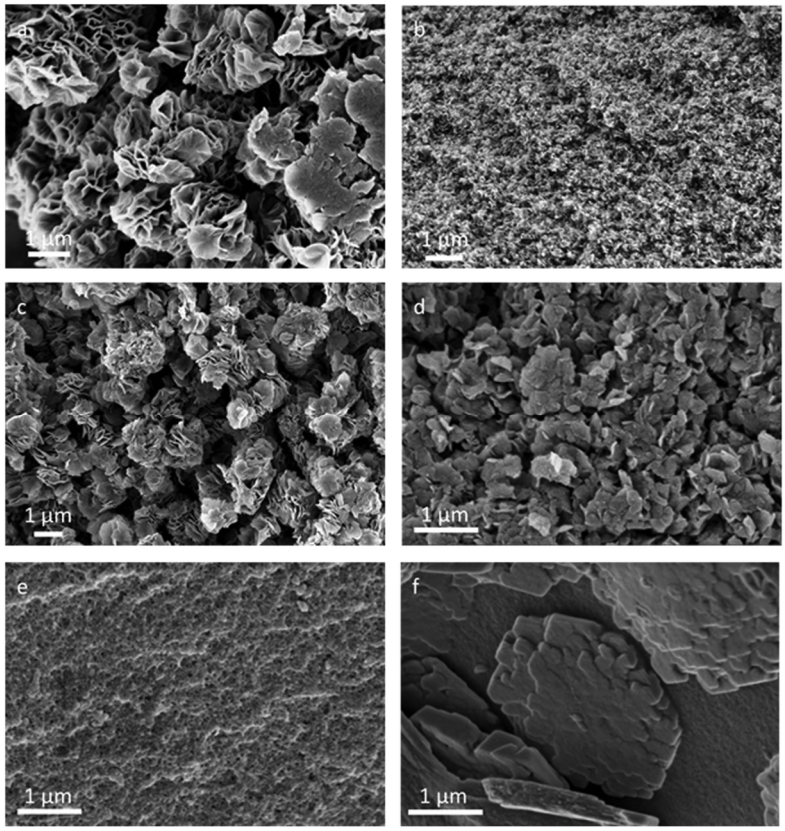

Fig. 3 Representative SEM images of carbon nitrides synthesized in (a) $LiCl/SnCl_2$, (b) $NaCl/SnCl_2$, (c) $KCl/SnCl_2$, (d) $CsCl/SnCl_2$, (e) $ZnCl_2/SnCl_2$ and (f) $SnCl_2$.[41]

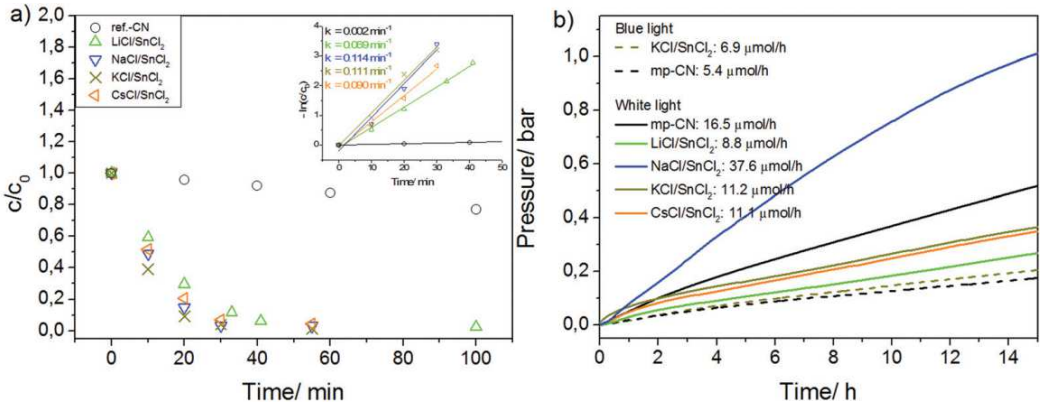

Fig. 4 (a) Dependence of Rhodamine B relative concentration (C/C_0) on irradiation time in the presence of photocatalysts obtained from $MCl/SnCl_2$ (M = Li, Na, K, Cs) salt melts; (b) Photocatalytic hydrogen evolution using $MCl/SnCl_2$-derived composites (M = Li, Na, K, Cs) and mp-CN as photocatalysts under different irradiation conditions.[41]

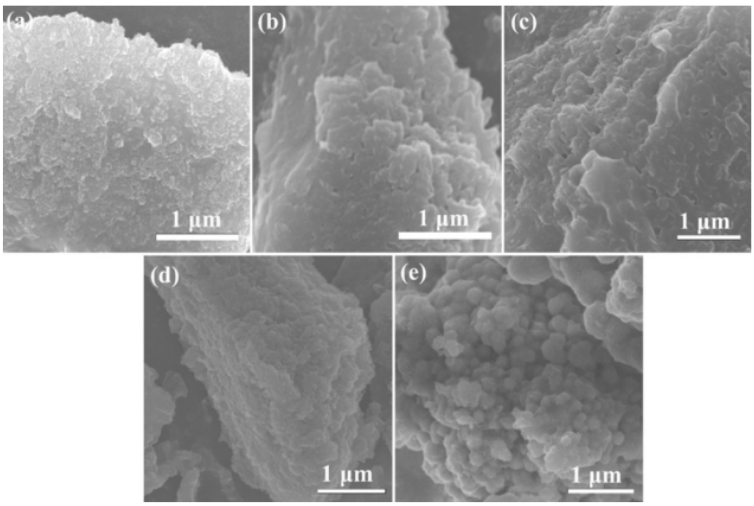

Fig. 5 SEM images of (a) 0 wt%, (b) 10 wt%, (c) 20 wt%, (d) 30 wt% and (e) 40 wt% g-C_3N_4/SiO_2/SnO_2 samples.[42]

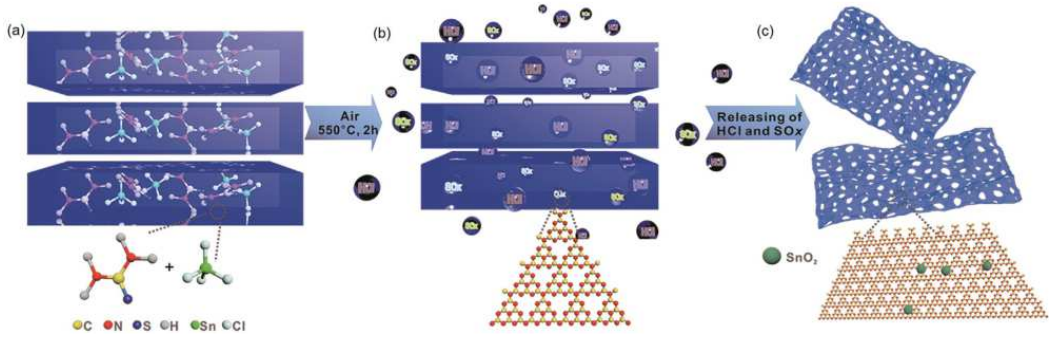

Fig. 6 Schematic illustration of the facile design of the highly macroporous g-C_3N_4 system. [44]

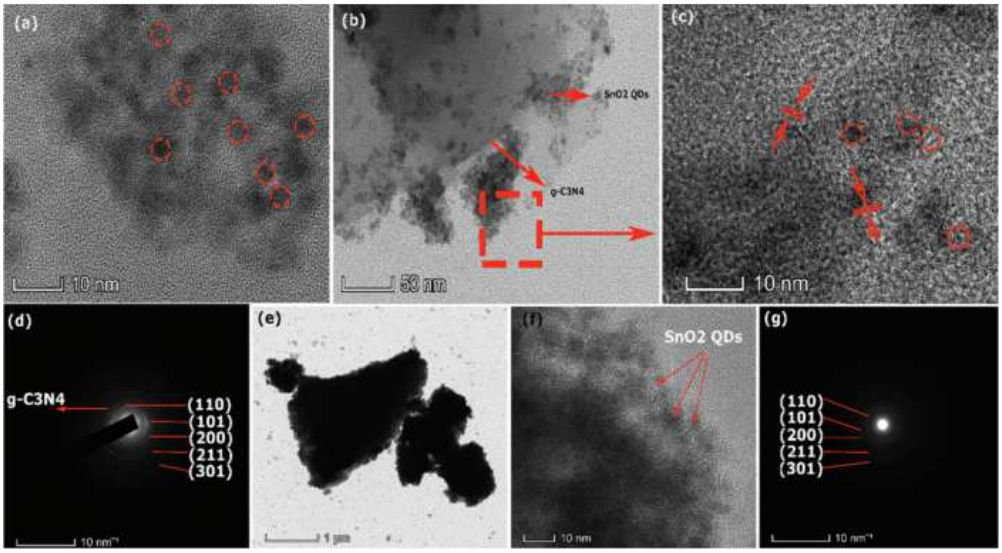

Fig. 7 TEM images of (a) pure SnO_2 QDs, (b, c) Low and HRTEM of SnO_2/g-C_3N_4 (1:2) nanohybrid, (d) SAED pattern of SnO_2/g-C_3N_4 (1:2) nanohybrid, (e, f) low and high resolution TEM image of SnO_2/g-C_3N_4 (5:1) nanohybrid, (g) SAED pattern of

SnO_2/g-C_3N_4 (5:1) nanohybrid.[35]

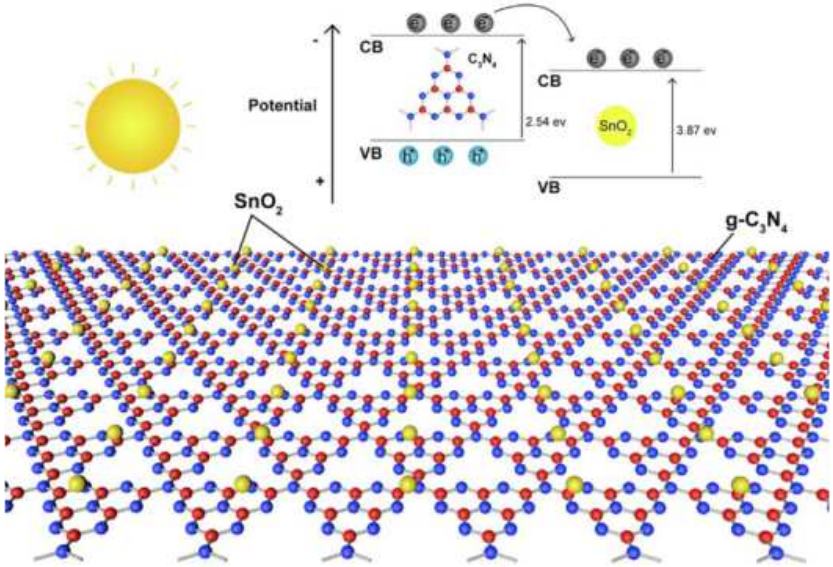

Fig. 8 Schematic of possible reaction mechanism for electron-hole transfer in SnO_2/g-C_3N_4 nanohybrid.[35]

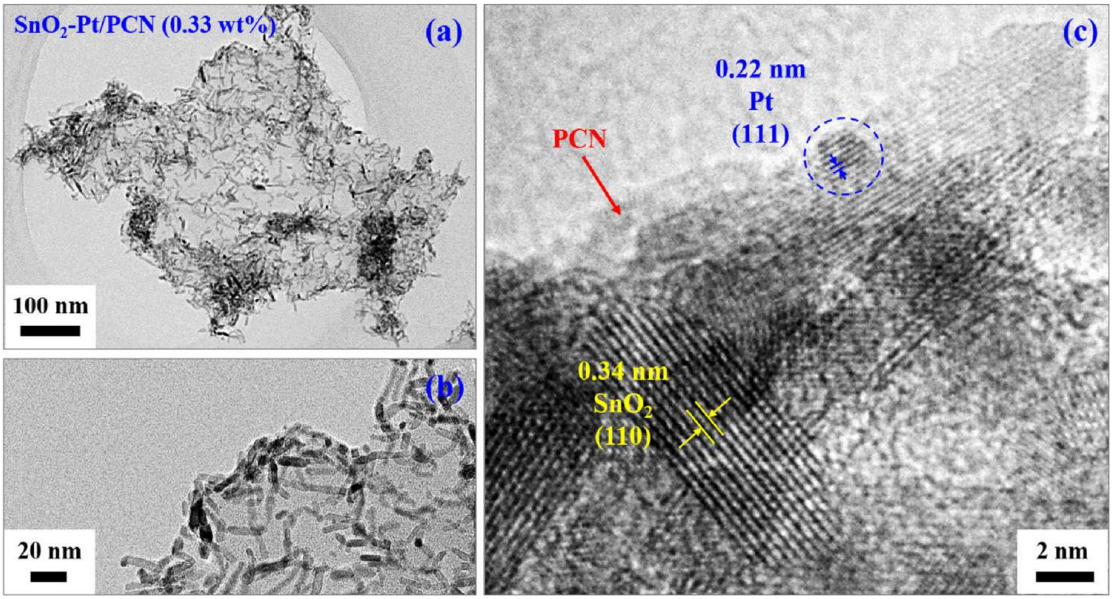

Fig. 9 (a) TEM and (b, c) HRTEM images of SnO_2-Pt/PCN (0.33 wt%). [57]

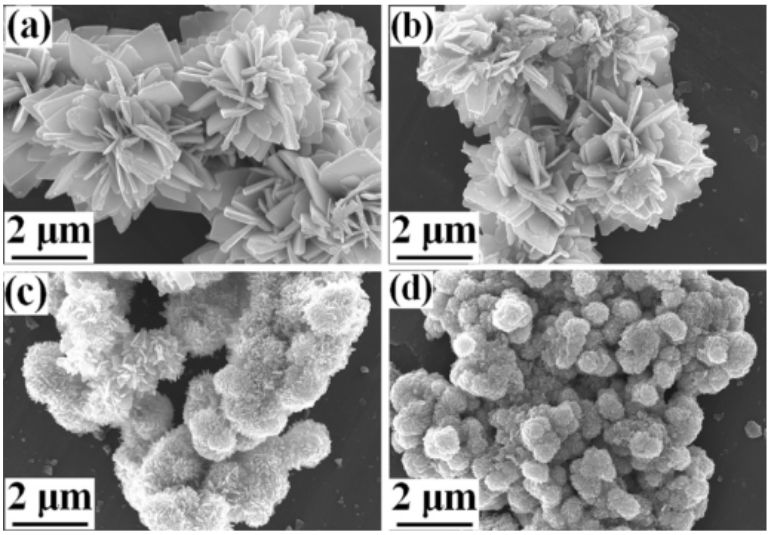

Fig. 10 SEM images of (a) pS, (b) 25%, (c) 50% and (d) 75% SnO_2/g-C_3N_4 heterostructures.[38]

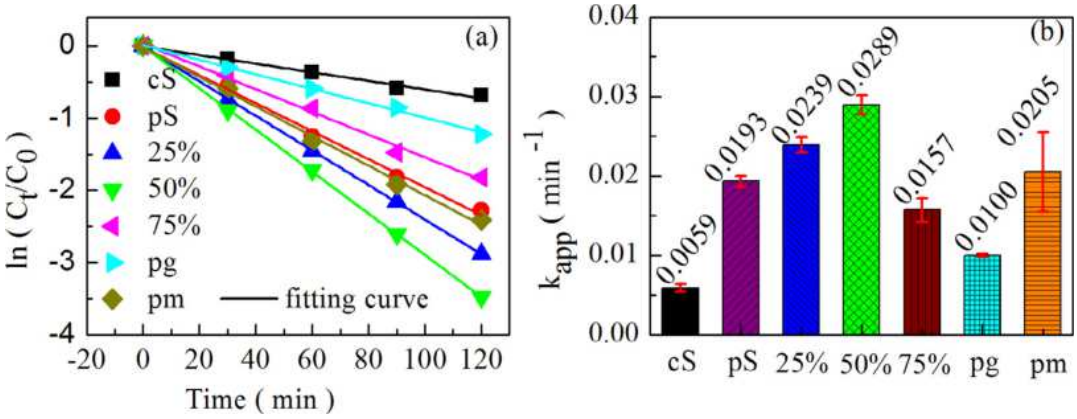

Fig. 11 RhB degradation curves of ln(C_t /C_0) versus time during photodegradation with all the samples, and k app values and stability of SnO_2/g-C_3N_4 heterostructures in the form of error bars.[38]

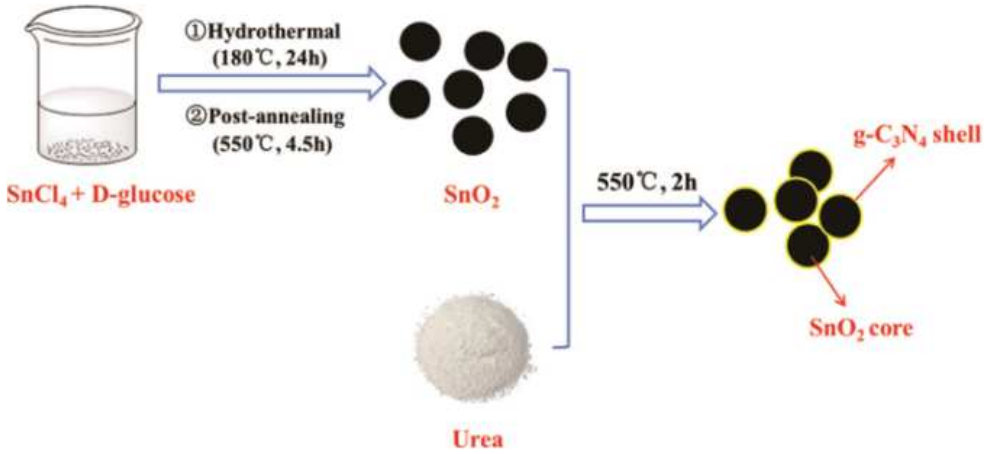

Fig. 12 Illustration of the preparation process of SnO_2@g-C_3N_4 core-shell structures.[42]

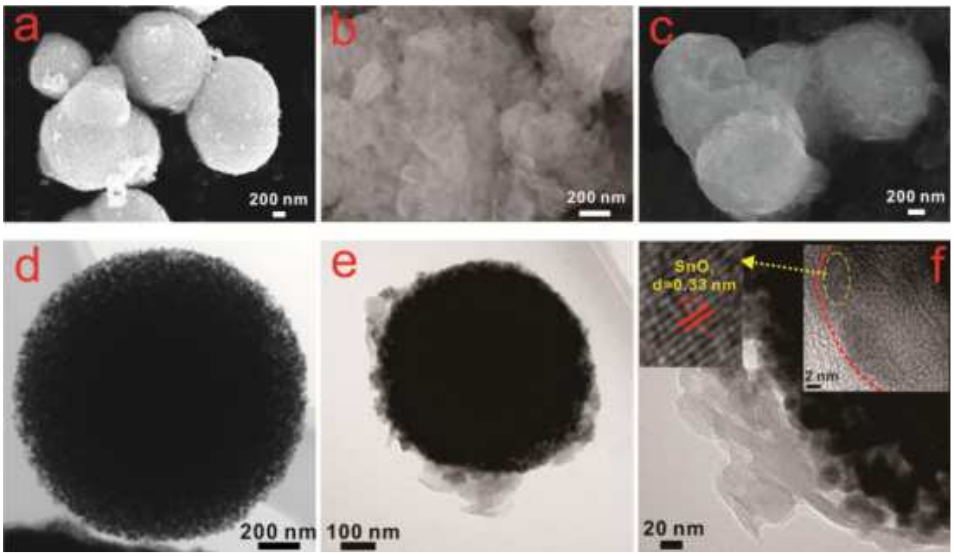

Fig. 13 SEM images of (a) SnO_2, (b) g-C_3N_4, (c) SnO_2@g-C_3N_4; TEM images of (d) SnO_2, (e, f) SnO_2@g-C_3N_4.[20]

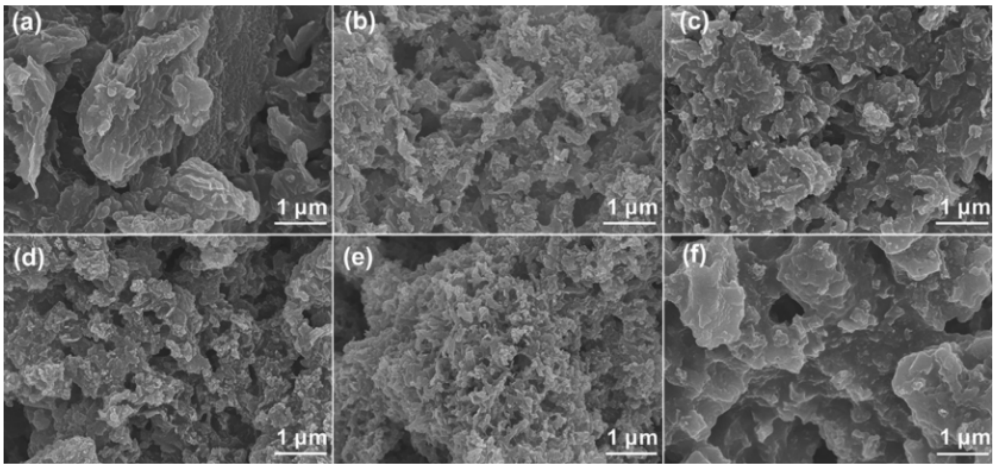

Fig. 14 SEM images of (a) pure g-C_3N_4, (b) Hybrid V, (c) Hybrid IV, (d) Hybrid III, (e) Hybrid II, and (f) Hybrid I.[45]

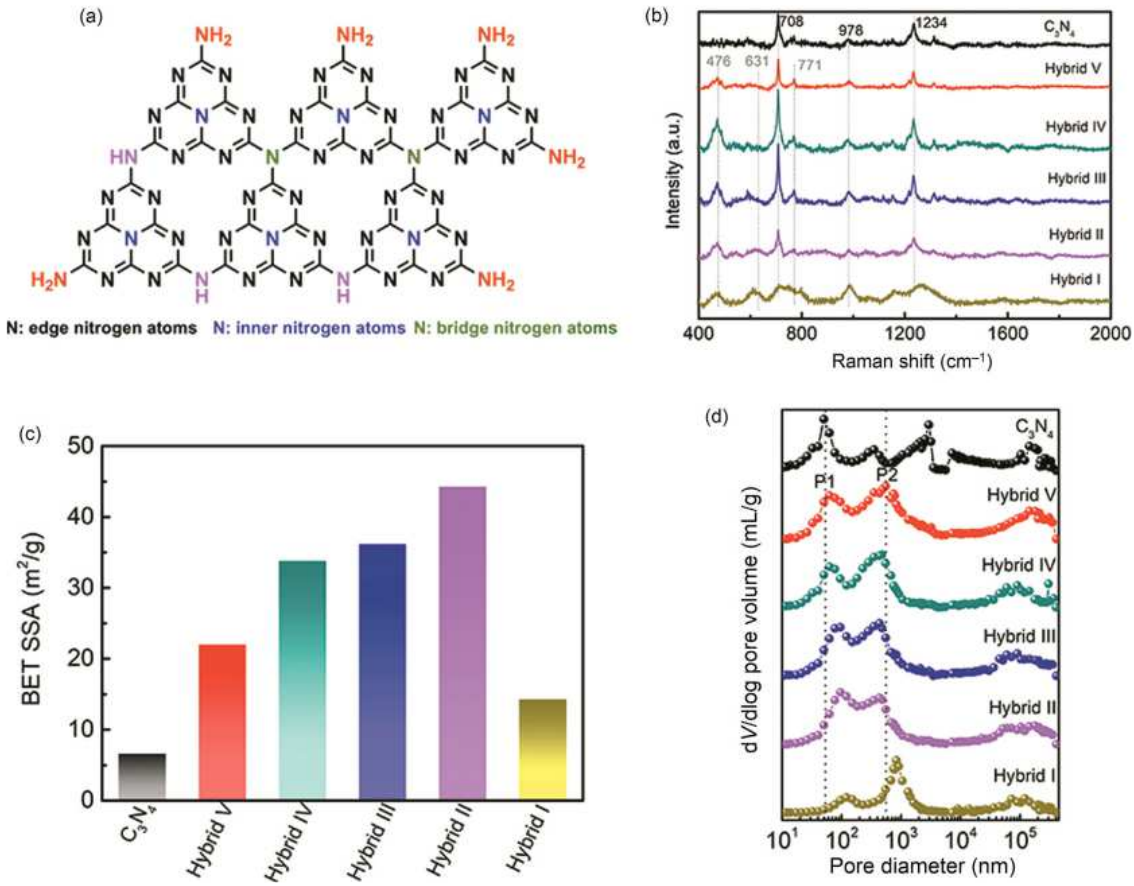

Fig. 15 (a) Supercell modal of monolayer g-C_3N_4 in a segment with SiC heptazine units, (b) Raman spectra, (c) the BET SSA, and (d) PSD of the as-prepared samples.[44]

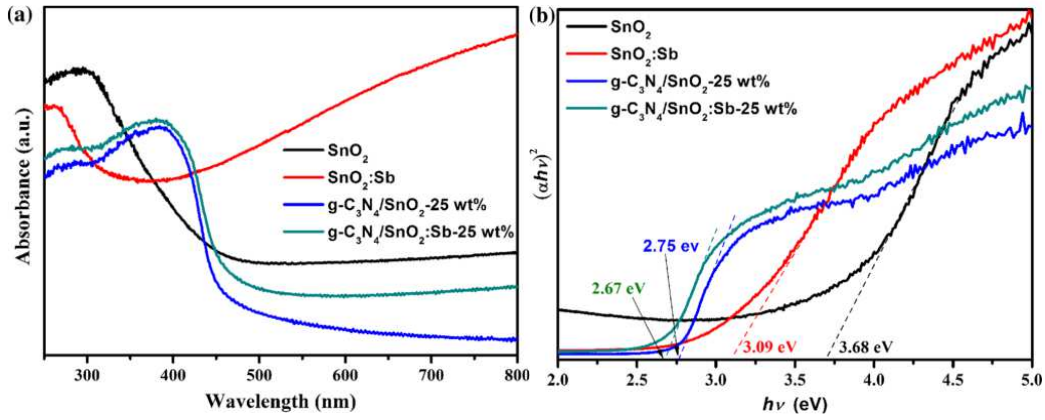

Fig. 16 (a) UV–vis diffuse reflectance spectra; (b) plots of the $(\alpha h\nu)^2$ versus $h\nu$ photon energy for bare SnO_2, SnO_2:Sb, g-C_3N_4/SnO_2-25 wt% and g-C_3N_4/SnO_2:Sb-25 wt% composites.[61]

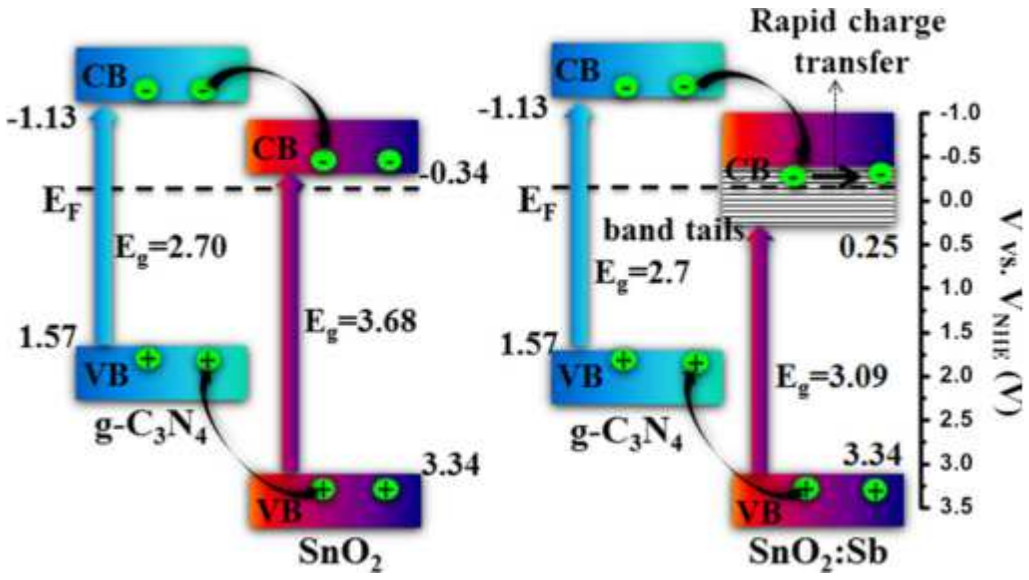

Fig. 17 Possible enhanced mechanism of photocatalytic activity for g-C_3N_4/SnO_2:Sb composites induced by doping Sb.[63]

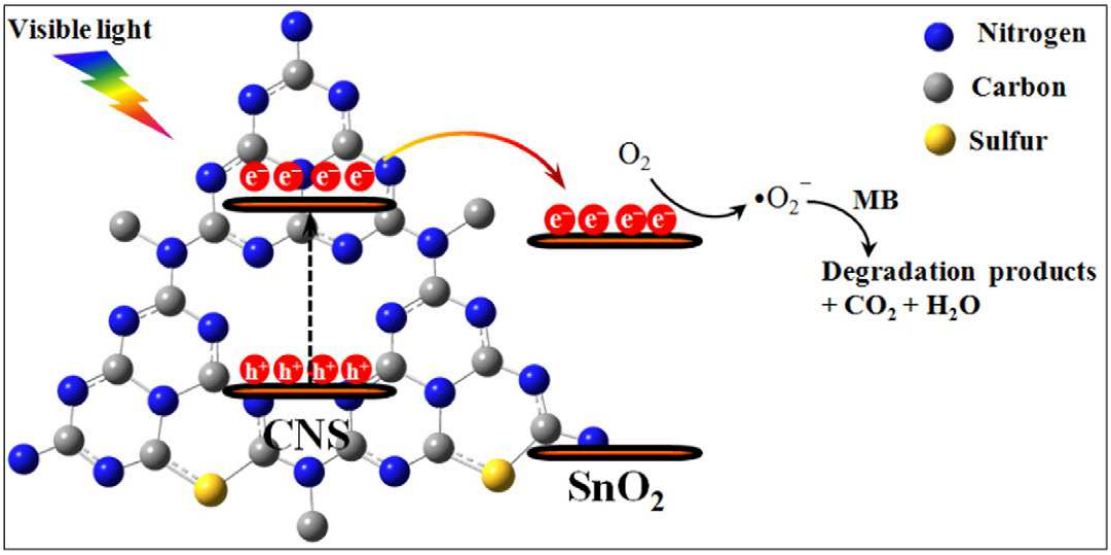

Fig. 18 The mechanism of visible light photocatalytic degradation of MB and the structure of SnO_2/CNS hybrid photocatalyst.[65]

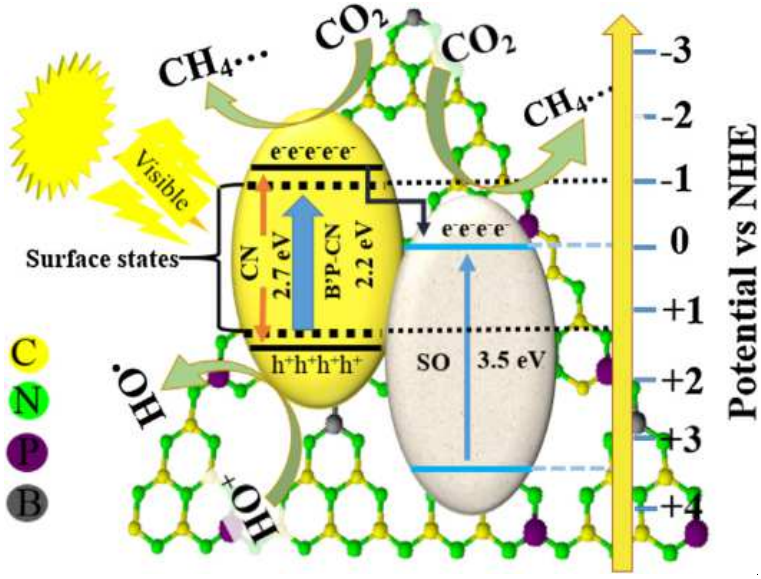

Fig. 19 Mechanism schematic of the photogenerated charge transfer and separation and photocatalytic reactions for CO_2 conversion and for pollutant degradation under visible-light irradiation on 6SO/0.12B-0.2P-CN. [66]

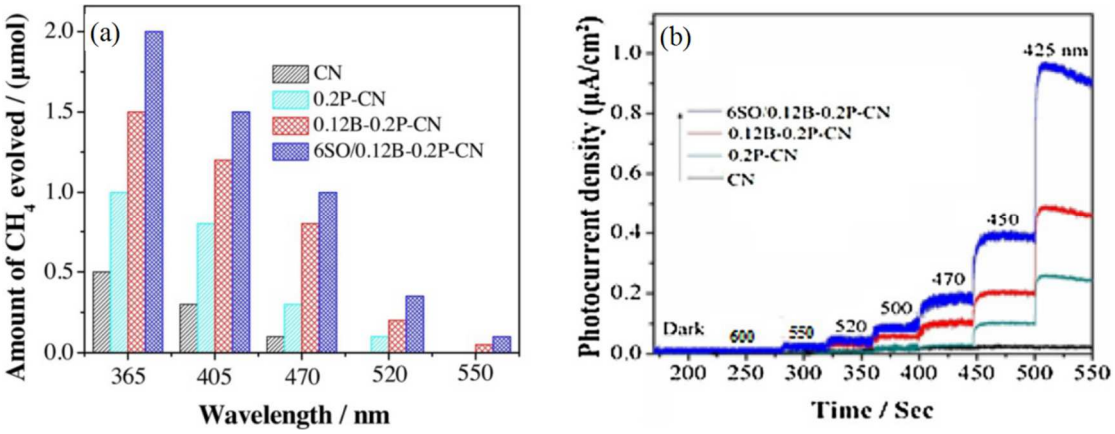

Fig. 20 (a) Single-wavelength activities for CO_2 conversion, and (b) single-wavelength photocurrent action spectra of CN, 0.2P-CN, 0.12B-0.2P-CN and 6SO/0.12B-0.2P-CN samples.[63]

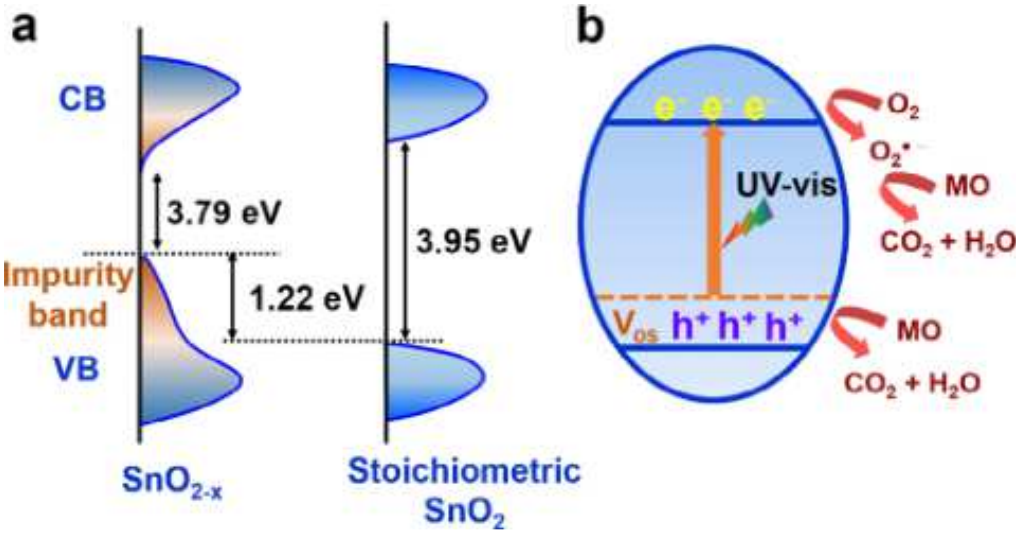

Fig. 21 (a) Schematic illustrations of the DOS for oxygen-deficient SnO_{2-x} and stoichiometric SnO_2, and (b) reaction mechanism over oxygen-deficient SnO_{2-x} photocatalyst under UV–visible irradiation.[76]

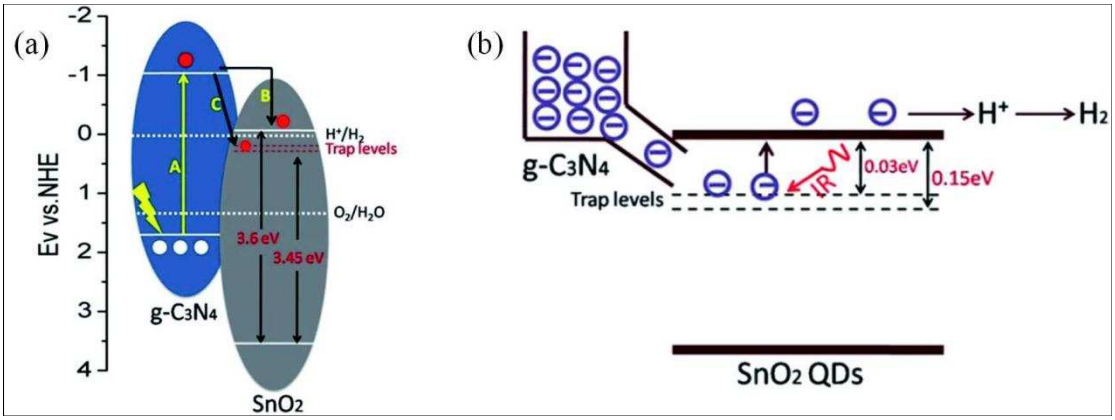

Fig. 22 (a) Photo-generated electron migration in SnO_2/g-C_3N_4 hybrids under visible light; (b) Re-excitation diagrams of localized electrons in SnO_2/g-C_3N_4 water for hydrogen generation from water photolysis by introducing infrared light.[51]

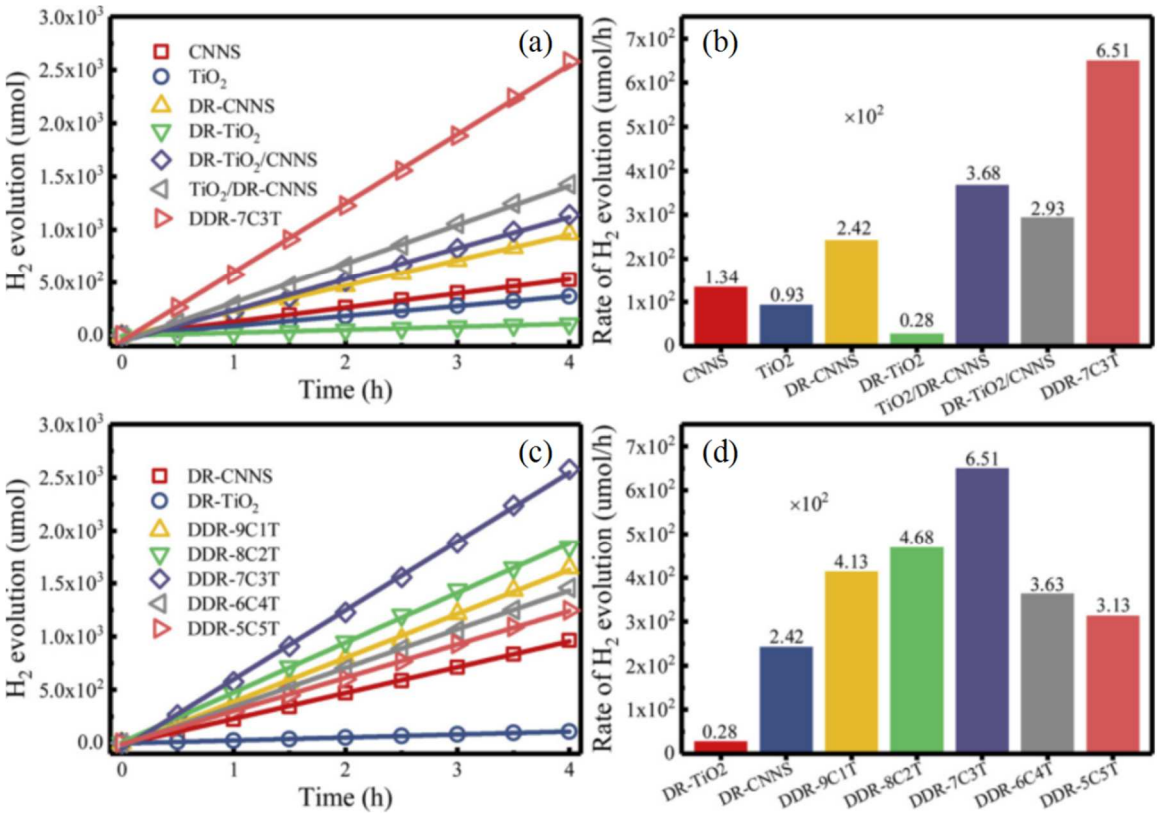

Fig. 23 (a, c) Photocatalytic H_2 evolution performances, and (b, d) evolution rate of different photocatalysts. [85]

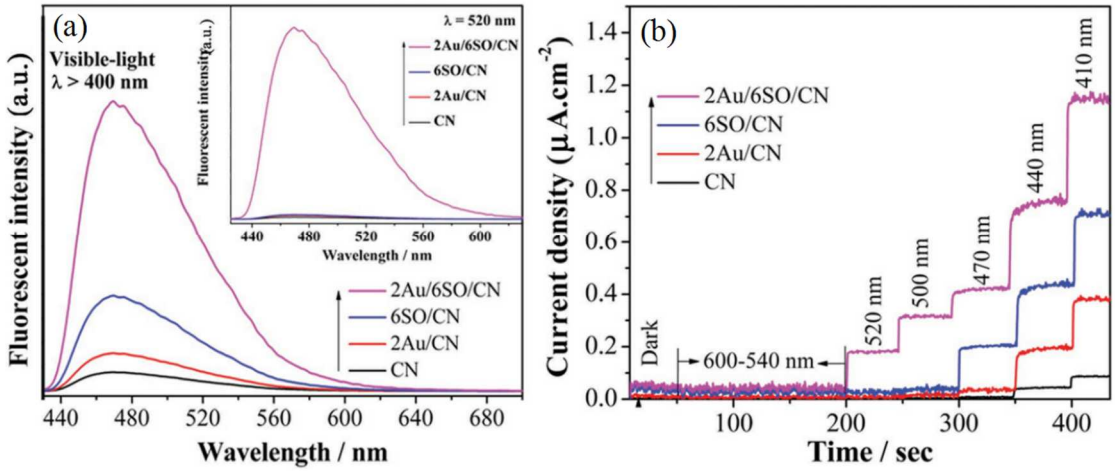

Fig. 24 Fluorescence spectra related to (a) the produced hydroxyl radicals and (b) photocurrent action spectra under different excitation wavelengths of CN, 2Au/CN, 6SO/CN, and 2Au/6SO/CN.[27]

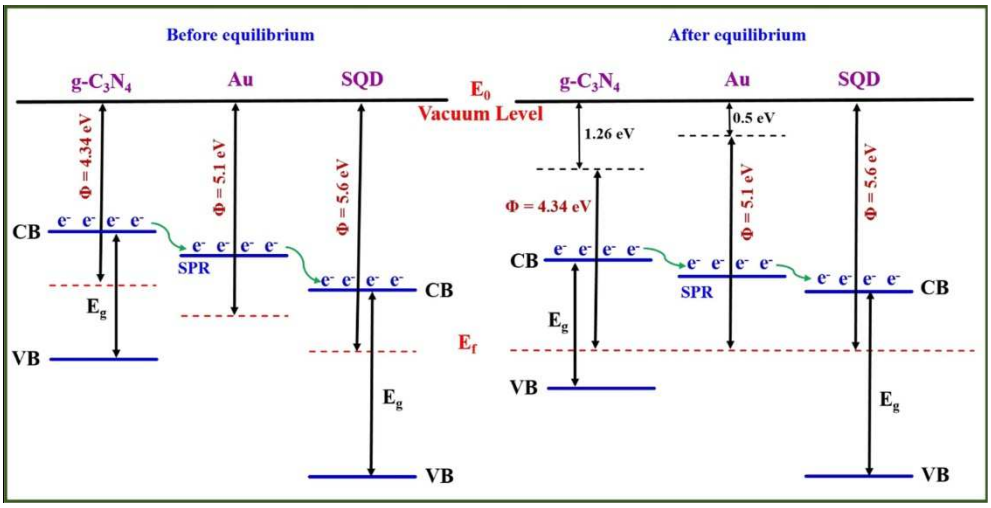

Fig. 25 Energy band structures of the g-CN/Au-SQD ternary nanocomposites. [89]

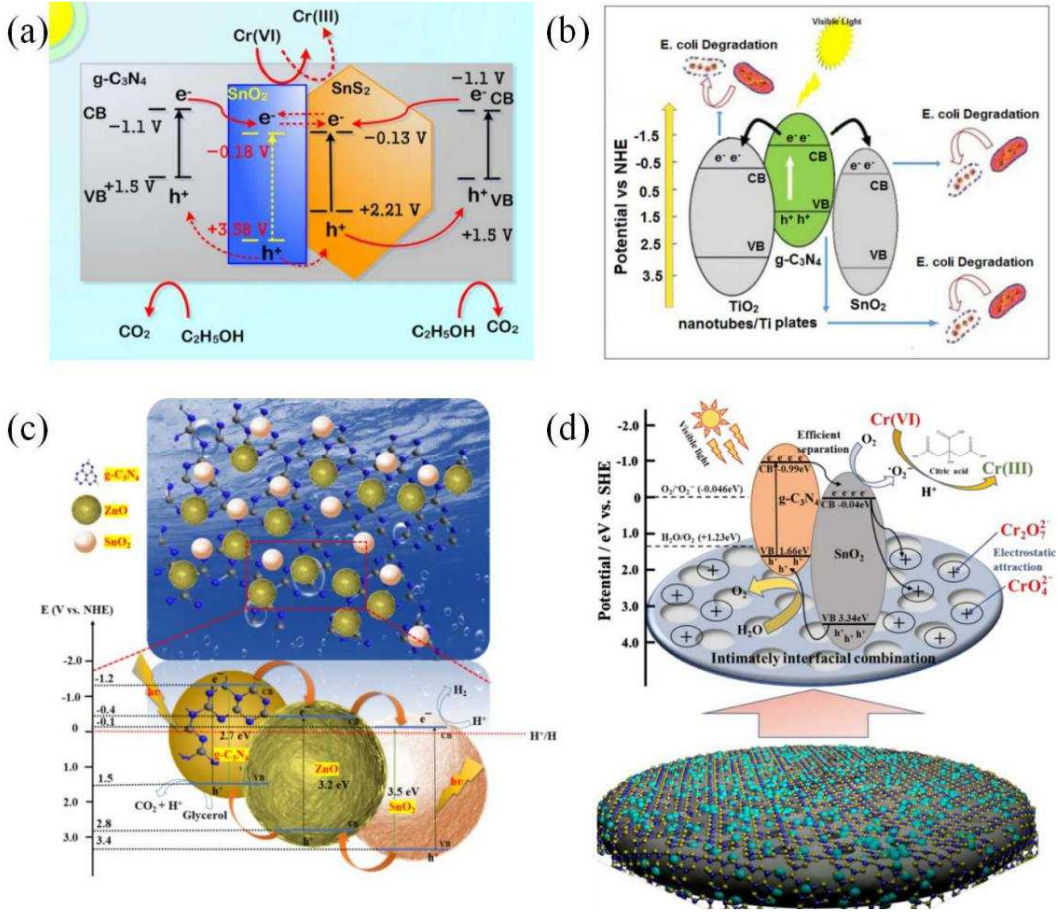

Fig. 26 (a) Diagram of photocatalytic reduction mechanism of Cr(VI) by g-C_3N_4/SnS_2/SnO_2[91]; (b) Schematic representations of antibacterial activity for g-C_3N_4-SnO_2/TiO_2 nanotubes/Ti plate toward E. coli under visible light irradiation[93]; (c) Schematic illustration of a plausible mechanism for photocatalytic H_2 production over SnO_2/ZnO/g-C_3N_4 catalyst under visible-light irradiation[94]; (d) Diagram description of the photocatalytic reduction enhancement mechanism for 30SnO_2/g-

C_3N_4/diatomite composite.[92]

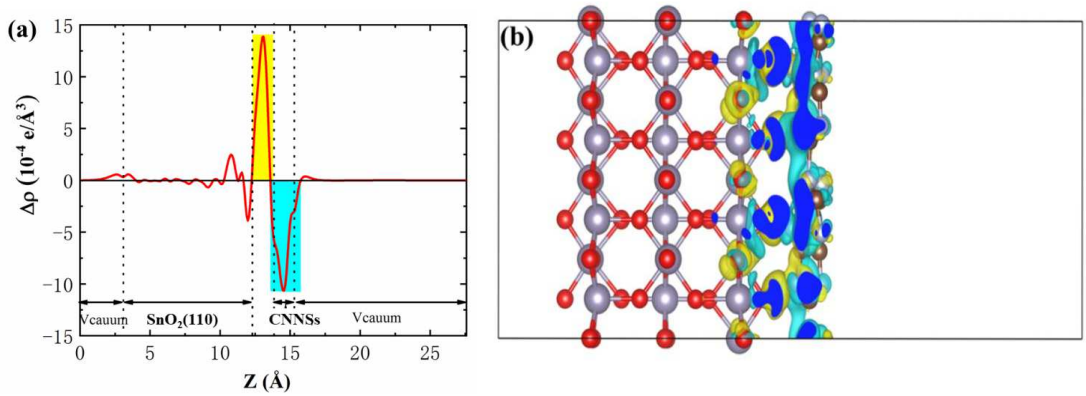

Fig. 27 (a) The average electron density difference (Δρ) along Z-direction for SnO_2(110)/CNNSs heterojunction. The yellow and cyan shaded areas indicate electron accumulation and donation, respectively. (b) The sides view of charge density difference.[96]

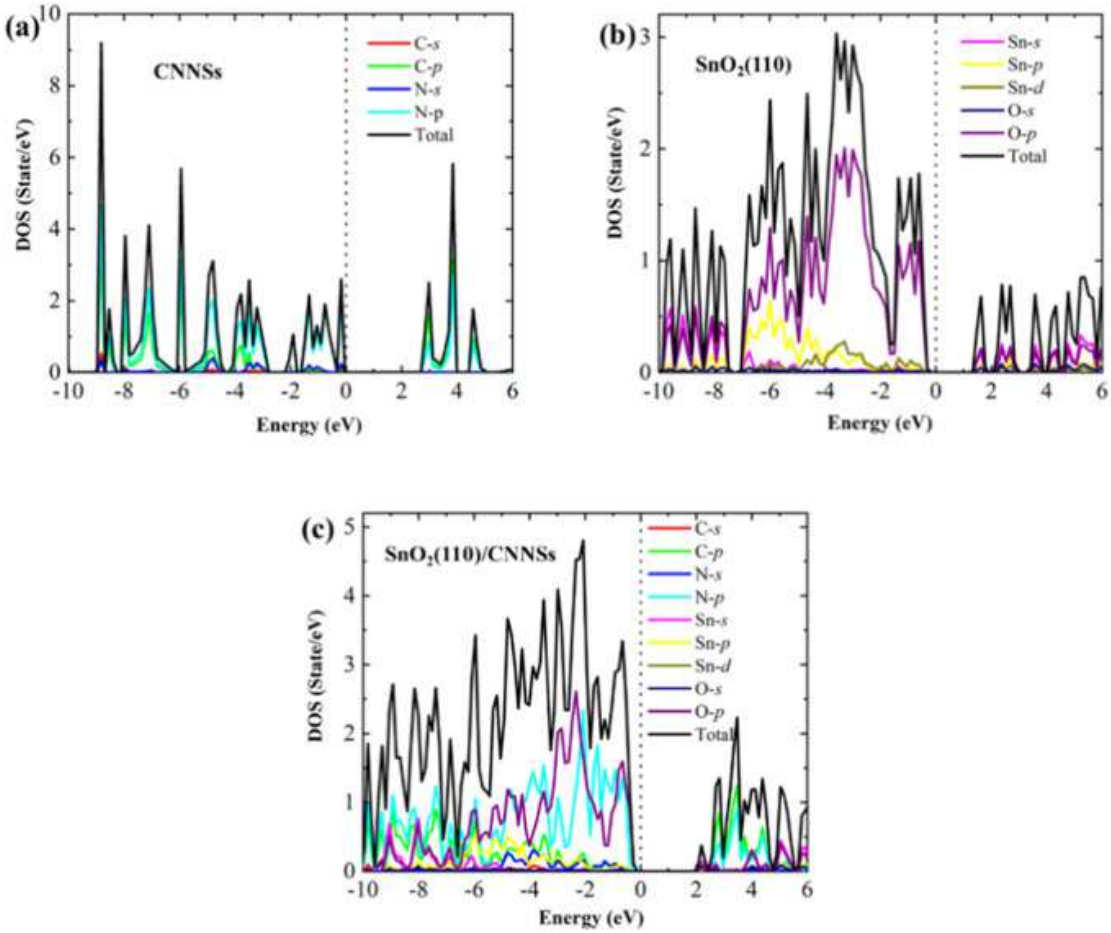

Fig. 28 The TDOS and corresponding PDOS of (a) CNNSs, (b) SnO_2(110) and (c) SnO_2(110)/CNNSs. The Fermi level is represented the by the dotted line.[96]

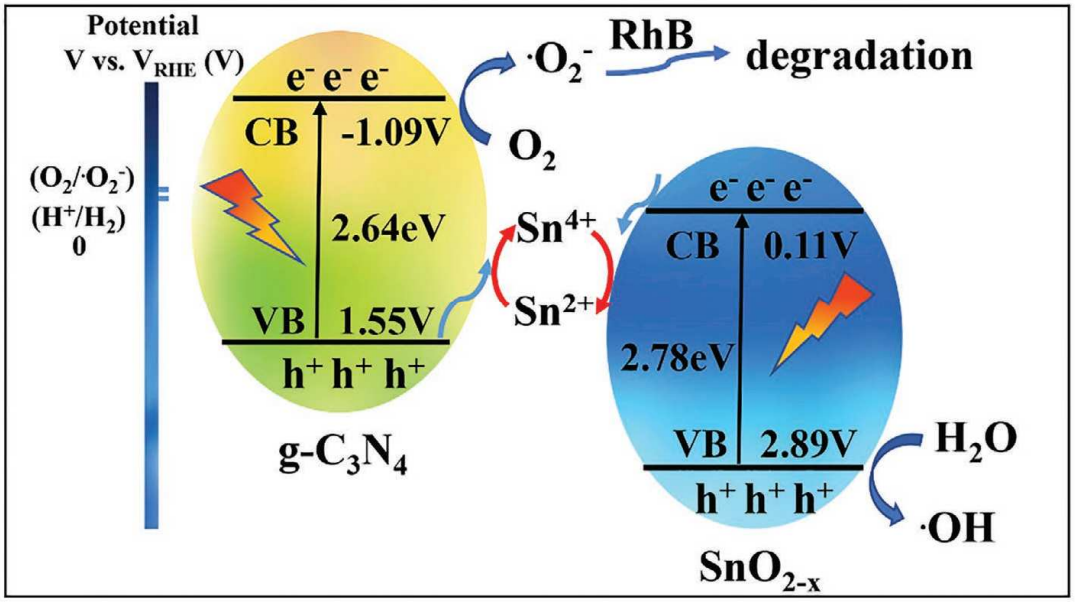

Fig. 29 Possible mechanisms for the photocatalytic process for defective flower-like SnO_2/g-C_3N_4.[102]

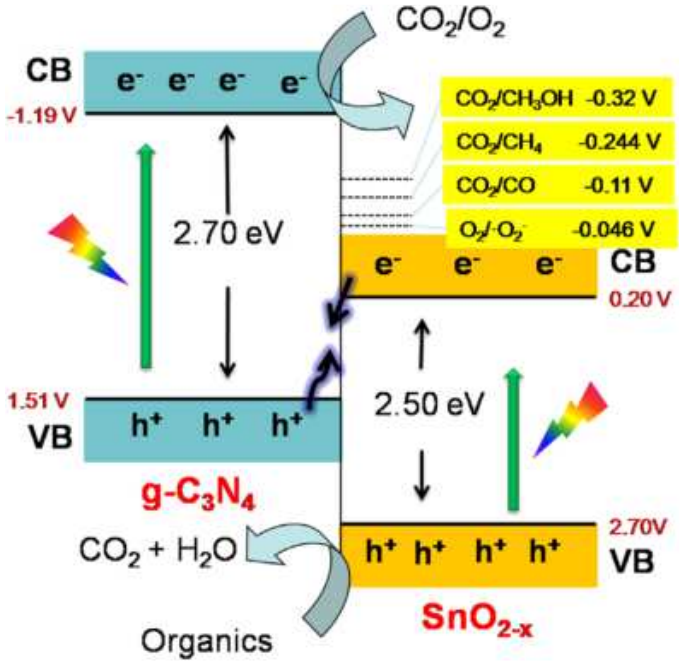

Fig. 30 Possible schemes for electron-hole separation and transport at the visible-light-driven SnO_{2-x}/g-C_3N_4 composite interface. [39]

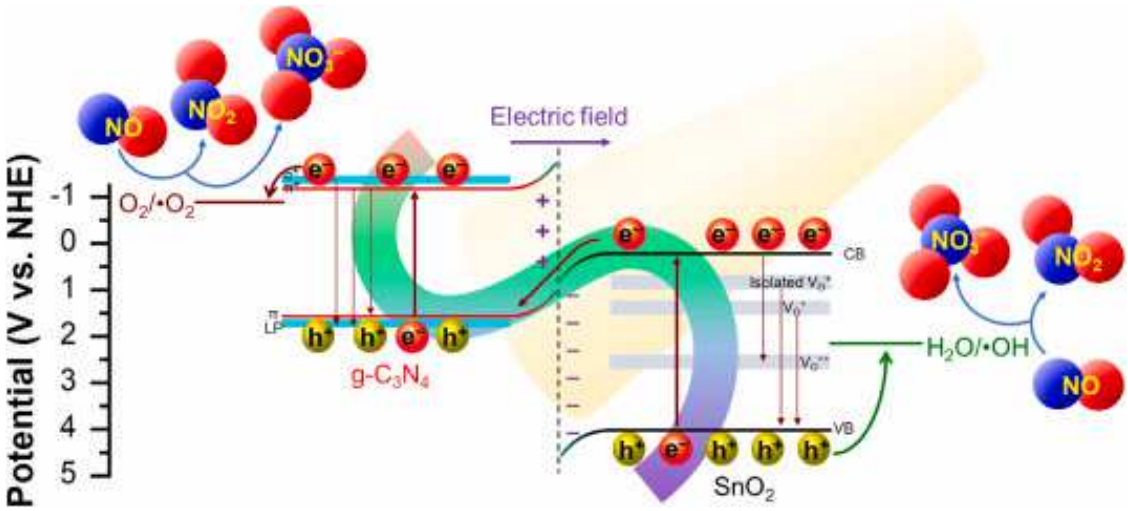

Fig. 31 Schematic of photocatalytic reactions for the NO removal over 2D/0D g-C_3N_4/SnO_2 S-scheme photocatalyst. [105]

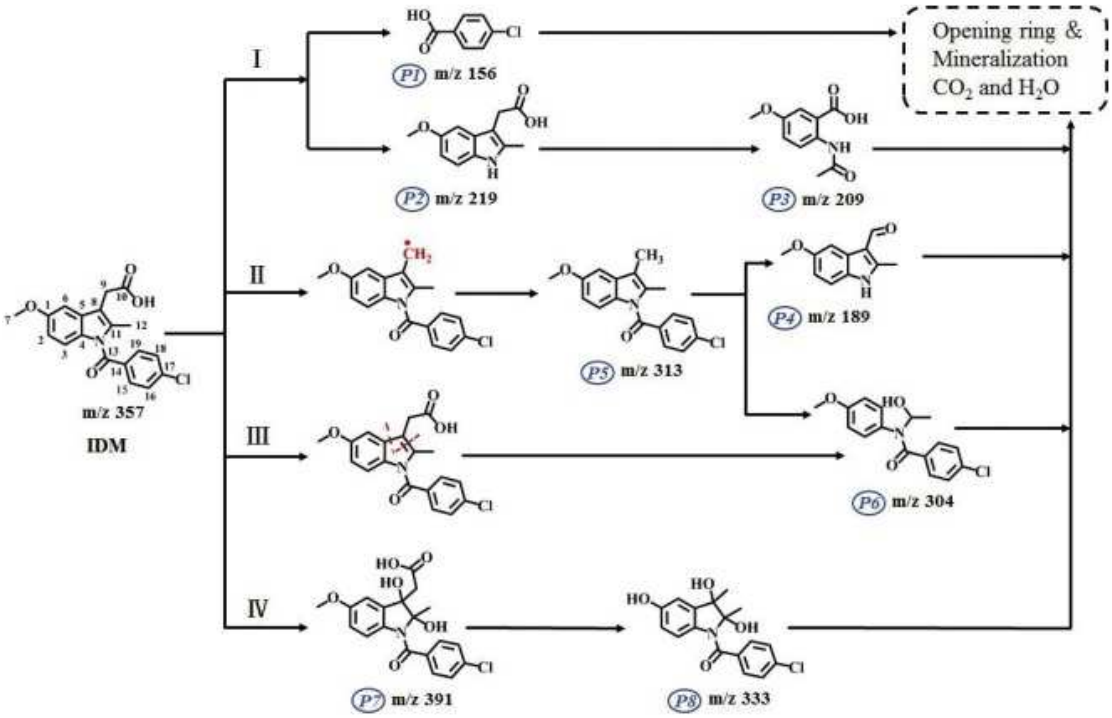

Fig. 32 Potential transformation pathways of IDM during the Carbon dots/g-C_3N_4/SnO_2 photocatalytic degradation process under visible light irradiation.[107]

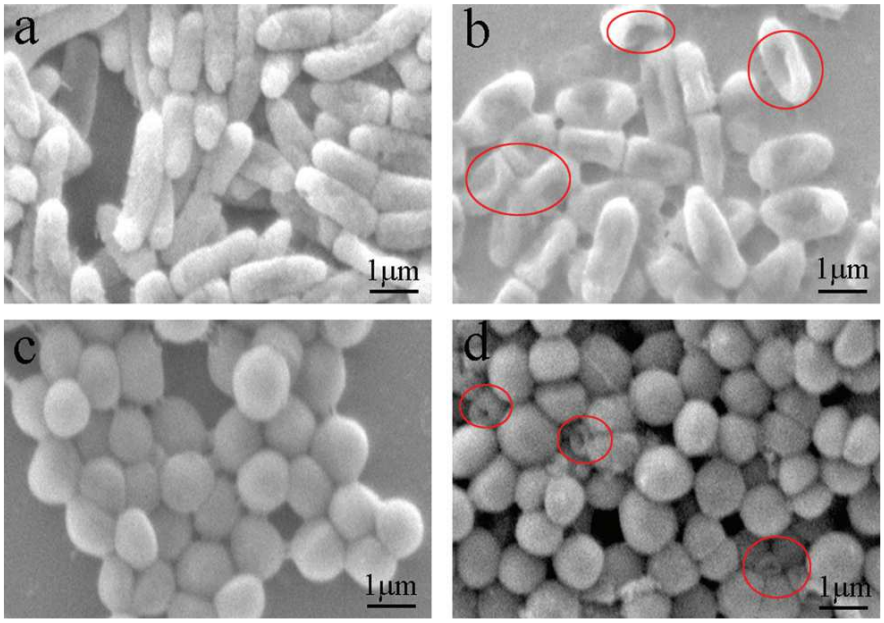

Fig. 33 (a, b) SEM images of E. coli untreated and treated with 1 wt% Fe-SCN under daylight lamp irradiation for 1 h; (c, d) SEM images of S. aureus untreated and treated with 1 wt% Fe-SCN under daylight lamp irradiation for 1 h.[112]

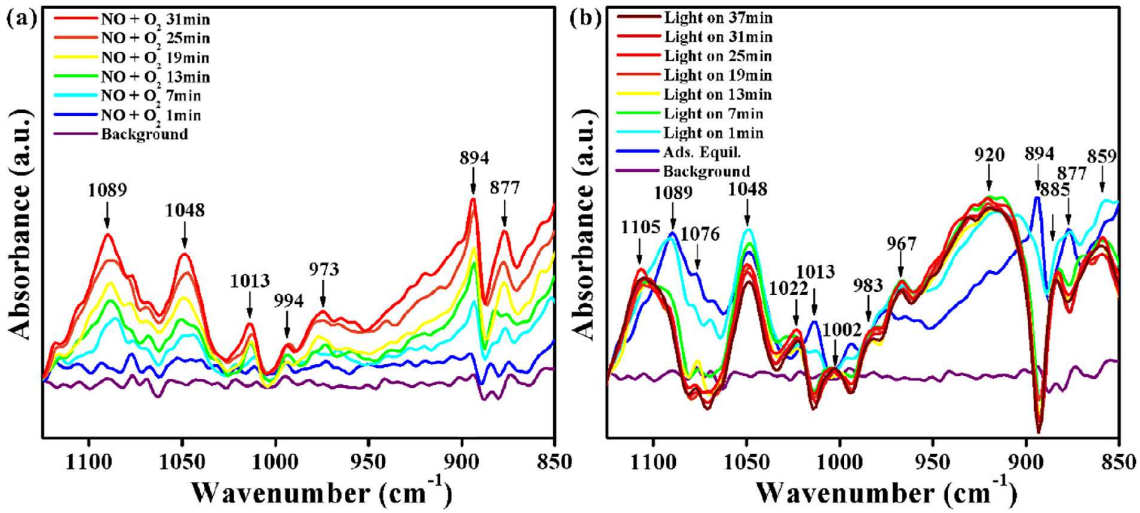

Fig. 34 In situ FTIR spectra of NO adsorption (a) and visible light reaction processes, (b) over 10% SnO_2/g-C_3N_4 photocatalysts. [113]

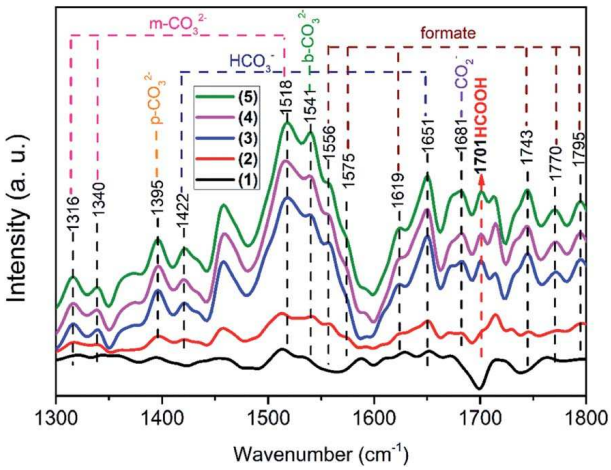

Fig. 35 In situ FT-IR spectra of the reaction of CO_2 and H_2O on diazanyl modified SnO_2/g-C_3N_4: (1) without CO_2 gas and irradiation; (2) under flowing CO_2 gas for 30 min without irradiation and with irradiation for (3) 20 min, (4) 40 min, and (5) 60 min.[115]

Table 1
Methods for synthesizing SnO_2/g-C_3N_4 photocatalysts

Photocatalyst	Preparation method	Main precursors		Additive	Processing temperature	Ref
SnO_2/g-C_3N_4	hydrothermal	$SnCl_4·5H_2O$	g-C_3N_4	—	/	[88]
SnO_2/g-C_3N_4	hydrothermal	$SnCl_4·5H_2O$	g-C_3N_4	melamine	180 °C for 16 h	[120]
SnO_2/g-C_3N_4	hydrothermal	$SnCl_4·5H_2O$	g-C_3N_4	—	120 °C for 11 h	[33]
SnO_2/g-C_3N_4	hydrothermal	$SnCl_4·2H_2O$	g-C_3N_4	—	180 °C for 24 h	[34]
SnO_2/g-C_3N_4	hydrothermal	$SnCl_4·5H_2O$, $N_2H_4·H_2O$	g-C_3N_4	—	180 °C for 24 h	[35]
g-C_3N_4/SnO_2:Sb	hydrothermal	$SnCl_4·5H_2O$, $SbCl_3$	g-C_3N_4	—	180 °C for 20 h	[63]
SnO_2/g-C_3N_4	hydrothermal	$SnCl_2·2H_2O$	g-C_3N_4	CTAB, HMT	in a microwave 93 °C for 1 h heat treat 450 °C for 2 h	[87]
SnO_2/g-C_3N_4	hydrothermal	SnO_2	g-C_3N_4, NH_4Cl	—	180 °C for 12 h	[36]
SnO_2/g-C_3N_4	solvothermal	stannic acetate	g-C_3N_4	dimethylsulfoxide	180 °C for 20 h	[121]
SnO_2/g-C_3N_4 SnO_{2-x}/g-C_3N_4	solvothermal	$SnCl_4·4H_2O$ $SnCl_2·2H_2O$	g-C_3N_4	— —	120 °C for 6 h	[79]
Sb-SnO_2/g-C_3N_4	Ultrasonic-assisting deposition method	Sb-SnO_2	g-C_3N_4	—	magnetic stirring for 2 h, heat treat 400 °C for 2 h	[62]
SnO_2/g-C_3N_4	Ultrasonic-assisting deposition method	SnO_2	g-C_3N_4	—	heat treat 400 °C for 1 h	[51]
SnO_2/g-C_3N_4	Ultrasonic-assisting deposition method	SnO_2	g-C_3N_4	—		[28]
SnO_2/g-C_3N_4	Ultrasonic-assisting deposition method	SnO_2	g-C_3N_4	HNO_3	vigorously stirred at 80 °C, heat treat 450 °C for 1 h	[32]
SnO_2/g-C_3N_4	Ultrasonic-assisting deposition method	SnO_2	g-C_3N_4	—	magnetic stirring for 2 h, heat treat 450 °C for 2 h	[26]
SnO_2/g-C_3N_4	Ultrasonic-assisting deposition method	SnO_2	g-C_3N_4	—	magnetic stirring for 2 h, heat treat 500 °C for 2 h	[27]
SnO_2/g-C_3N_4	Ultrasonic-assisting deposition method	SnO_2	g-C_3N_4	—	magnetic stirring for 12 h	[106]
SnO_2/g-C_3N_4	Ultrasonic-assisting deposition method	SnO_2	g-C_3N_4	—	magnetic stirring for 24 h, heat treat 400 °C for 1 h	[29]

SnO_2/g-C_3N_4	Sol-gel method	$SnCl_2 \cdot 2H_2O$,	g-C_3N_4	TEOS	heat treat 550 °C for 4 h	[42]
SnO_2/g-C_3N_4	Solid-phase method	MCl/$SnCl_2$ (M = Li, Na, K, Cs) salt melts	DCDA	—	heat treat 550 °C for 6 h	[41]
SnO_2@g-C_3N_4	Solid-phase method	SnO_2 microspheres	melted urea	—	heat treat 550 °C for 2 h	[20]
SnO_2/g-C_3N_4	Solid-phase method	SnO_2	DCDA	—	heat treat 550 °C	[40]
SnO_2/g-C_3N_4	Solid-phase method	SnO_2	melamine	—	heat treat 550 °C for 2 h	[38]
SnO_{2-x}/g-C_3N_4	Solid-phase method	$Sn_6O_4(OH)_4$	g-C_3N_4	—	heat treat 400 °C for 2 h	[39]
SnO_2/g-C_3N_4	In situ co-pyrolysis method	$SnCl_4 \cdot 5H_2O$	thiourea	—	heat treat 550 °C for 2 h	[44]
SnO_2/g-C_3N_4	In situ co-pyrolysis method	tin, hydrochloric acid	urea	ammonium hydroxide	in a microwave oven for 30 min	[45]
SnO_{2-x}/g-C_3N_4	In situ co-pyrolysis method	$Sn(OH)_4$	melamine	—	magnetic stirring for 24 h, heat treat 520 °C for 4 h	[46]
SnO_2/g-C_3N_4	In situ co-pyrolysis method	$SnCl_4 \cdot 5H_2O$	thiourea	—	magnetic stirring at 90 °C, heat treat 535 °C for 3 h	[40]
SnO_2/g-C_3N_4		$SnCl_2$	g-C_3N_4	NaOH	freezing at −20 °C, heat treat 450 °C	[47]
SnO_2/g-C_3N_4		SnI_4	g-C_3N_4	—	magnetic stirring at 70 °C for 5 h	[113]
SnO_2/g-C_3N_4		$SnCl_4 \cdot 5H_2O$	urea	hydrazine	magnetic stirring at 100 °C for 18 h	[54]

Table 2
Representative summary of recent studies on SnO_2/g-C_3N_4 heterojunction and their photocatalytic properties

Hybrid photocatalyst	Target	Dosage	Efficiency	Efficiency of reference photocatalyst	Enhancement factor over reference photocatalyst	Light source	Stability	Refs.
g-C_3N_4/SnO_2	250ml 2.5×10^{-5}M RhB	0.1g	90% in 60min	g-C_3N_4:66% in 60min SnO_2:25% in 60min	9.3 2.1	500W tungsten lamp	-	[48]
g-C_3N_4/SnO_2	100ml of aqueous methanol	0.1g	H_2:132 μmol h^{-1}	g-C_3N_4:H_2:10 μmol h^{-1} SnO_2:H_2:0 μmol h^{-1}	-	300W Xe lamp (λ＞420 nm)	25h	[32]
Ag@SnO_2-g-C_3N_4	25 mg L^{-1} 2-CP	4 g L^{-1}	42% in 60min	-	-	150W Xe lamp (λ＞420 nm)	-	[88]
	10 mg L^{-1} MB	2.5 mg/20 ml	6mM Ag@SnO_2-g-C_3N_4:99.40% in 90min	3Mm Ag@SnO_2-g-C_3N_4: 98.36% in 90min 1mM Ag@SnO_2-g-C_3N_4: 89.67% in 90min	-	400W Xe lamp (λ＞500 nm)	6h	
	10 mg L^{-1} CR		6mM Ag@SnO_2-g-C_3N_4:98% in 60min	-	-			
	5 mg L^{-1} RhB		6mM Ag@SnO_2-g-C_3N_4:94% in 240min	-	-			
SnO_2/GL-C_3N_4 (NLs/NLs)	10 mg L^{-1} RhB	1 g L^{-1}	92% in 3h	GL-C_3N_4:36% in 3h SnO_2:10% in 3h	2.5 9	300W Xe lamp (λ＞420 nm)	12h	[36]

$g\text{-}C_3N_4/SnO_2$:Sb	100 ml 5.0×10^{-5}M RhB	0.1 g	$g\text{-}C_3N_4/SnO_2$:Sb-25%:92% in 60min	$g\text{-}C_3N_4/SnO_2$-25%: 71% in 60min	-	300W Xe lamp (λ＞420 nm)	4h	[63]
$Au/SnO_2/g\text{-}C_3N_4$	80 ml distilled water and 20ml methanol	0.1 g	H_2:770 μmol g^{-1} h^{-1}	$g\text{-}C_3N_4$:H_2:11 μmol g^{-1} h^{-1} Au/CN:H_2:112 μmol g^{-1} h^{-1} SO/CN:H_2:130 μmol g^{-1} h^{-1}	-	300W Xe lamp (λ＞420 nm)	30h	[27]
SnO_2/C_3N_4	5ml 10mg L^{-1} RhB	5mg	-	-	-	12W LED module emitting at 420nm	-	[41]
	Pt, TEOA	-	($KCl/SnCl_2$)H_2:6.9 μmol h^{-1}	mp-CN:H_2:5.4 μmol g^{-1} h^{-1}	-	12W blue LED array(maximum at 420 nm)	＞20h	
		-	($NaCl/SnCl_2$)H_2:37.6 μmol h^{-1}	mp-CN:H_2:16.5 μmol g^{-1} h^{-1}	-	50W white LED array		
$SnO_2/g\text{-}C_3N_4$	15ml 10 mg L^{-1} MO	15mg	≈100% in 100min	$g\text{-}C_3N_4$:15% in 100min SnO_2:0% in 100min	17 89	500W Xe lamp (λ＞420 nm)	400min	[120]
	15ml 10 mg L^{-1} RhB	15mg	98.7% in100min	-	-			
$SnO_2/g\text{-}C_3N_4$	50ml 10^{-5} mol L^{-1} RhB	10mg	97.5% in 15min	SnO_2:4.4% in 15min Degussa P25:38.0% in 15min	-	350W Xe lamp (λ＞420 nm)	90min	[121]
$SnO_2/g\text{-}C_3N_4$	AP	-	-	-	-	-	-	[40]
$SnO_{2-x}/g\text{-}C_3N_4$	20 mg L^{-1} TC	1 g L^{-1}	83% in 120min	$g\text{-}C_3N_4$:55% in 120min SnO_{2-x}:10% in 120min $SnO_2/g\text{-}C_3N_4$	- - 1.27	35W LED track light (λ=450±24 nm)	8h	[79]

	10 mg L^{-1} RhB	1 g L^{-1}	≈100% in 15min	$g\text{-}C_3N_4$ SnO_{2-x} $SnO_2/g\text{-}C_3N_4$	1.8 1.4 1.74			
	50ml E.*coli* suspension	30mg	≈100% in 30min	-	-			
$SnO_2/g\text{-}C_3N_4$	90 ml deionized water and 10ml triethanolamine	100mg	H_2:11.3 μmol 3h H_2:21.1 μmol 3h	$g\text{-}C_3N_4$:H_2:6 μmol 3h SnO_2:H_2:0 μmol 5h $g\text{-}C_3N_4$:H_2:10 μmol 3h	- - -	300W Xe lamp (λ＞420 nm) With a heat insulation filer 300W Xe lamp (λ＞420 nm)	- - -	[51]
$SnO_2/g\text{-}C_3N_4$	10 mg L^{-1} MO	1 g L^{-1}	-	$g\text{-}C_3N_4$: ignore SnO_2:ignore	-	2×36W fluorescent lamp with a 420 nm cutoff filter	640min	[28]
$SnO_{2-x}/g\text{-}C_3N_4$	80ml 10 mg L^{-1} RhB	40mg	0.0226min^{-1}	$g\text{-}C_3N_4$ SnO_2	5.79 32.28	A 30W LED lamp	-	[46]
SnO_2-ZnO QDs/$g\text{-}C_3N_4$	100ml RhB	40mg	≈100% in 60min	$g\text{-}C_3N_4$:≈100% in 130min $ZnO/g\text{-}C_3N_4$:≈100% in 100min	5.11 2.12	300W Xe lamp With a glass filter(remove UV＜390 nm and IR＞700 nm)	240min	[94]
	Pure water	-	H_2:239.29 μmol g^{-1}	-	-	300W Xe lamp	25h	

	50ml of 5% aqueous glycerol	100 mg L^{-1}	H_2:13673.61 μmol g^{-1} 5h	g-C_3N_4:H_2:6017.72 μmol g^{-1} 5h ZnO/g-C_3N_4:H_2:12785.54 μmol g^{-1} 5h	2.27 1.06	(λ＞400 nm)		
DR-TiO2/DR-CNNs	TEOA aqueous solution(10 vol.%) with Pt(3 wt.%)	10mg	H_2:651.79 μmol h^{-1}	DR-CNNs:H_2:242.11 μmol h^{-1} CNNs:H_2:134.18 μmol h^{-1} DR-TiO_2:H_2:28.1 μmol h^{-1} DR-TiO_2/CNNs:H_2:293.48 μmol h^{-1} TiO_2/DR-CNNs:H_2:368.59 μmol h^{-1}	2.7 - 23.3 - -	300W Xe lamp	＞100h	[85]
TiO_2/g-C_3N_4/Ag	80 ml deioniaed water and 20ml of methanol	0.1g	H_2:169.46 μmol g^{-1} h^{-1}	g-C_3N_4:H_2:12.15 μmol g^{-1} h^{-1} T/CN:H_2:28.38 μmol g^{-1} h^{-1} Ag/CN:H_2:36.79 μmol g^{-1} h^{-1} Au/CN:H_2:80.37 μmol g^{-1} h^{-1} Au/T/CN:H_2:215.63 μmol g^{-1} h^{-1} Pt/CN:H_2:253.68 μmol g^{-1} h^{-1} Pt/T/CN:H_2:519.73 μmol g^{-1} h^{-1}	-	300W Xe lamp (λ＞420 nm)	30h	[26]
	8ml water (with or without 2ml methanol) +CO_2	0.2g	CH_4	g-C_3N_4(with methanol) g-C_3N_4(without methanol)	2.2 9.5			
SnO_2 QDs	50ml 20mg L^{-1} MO	0.05g	-	P25 TiO2 Commercial SnO2	182.13 259.26	300W Xe lamp (λ＞400 nm)	-	[122]

SnO_2/g-C_3N_4	10ml 5mg L^{-1} RhB	5mg	98.73% in 90min	g-C_3N_4:12.63% in 90min SO/CN-1:3:89.78% in 90min SO/CN-1:4:71.57% in 90min SO/CN-3:1:41.05% in 90min SO/CN-5:1:26.31% in 90min	-	65W CFL lamp (λ＞400 nm)	450min 5 cycles	[106]
	10ml 45mg L^{-1} RbX	5mg	93.75% in 80min	g-C_3N_4:8.75% in 80min SO/CN-1:3:70% in 80min SO/CN-1:4:46.25% in 80min SO/CN-3:1:28.75% in 80min SO/CN-5:1:20% in 80min	-		400min 5 cycles	
g-C_3N_4/Au-SnO_2	-	-	99% in 40min	Au-SQDs:53% in 40min g-C_3N_4:65% in 40min CNAS-10: 85% in 40min CANS-30: 92% in 40min	5.21 3.6	-	200min 5 cycles	[89]
SnO_2@g-C_3N_4	50ml 1×10^{-5}mol/L MO	20mg	-	-	-	500W Xe lamp With a 420nm cutoff filter	480min 4 cycles	[20]
SnO_2/SnS_2/g-C_3N_4	100ml 20mg L^{-1} Cr(VI)	20mg	98.5% in 60min	g-C_3N_4:2.1% in 60min SnS_2/SnO_2:45.2% in 60min Mechanical mixing:59.4% in 60min	-	A batch photocatalytic device (500W halogen lamp, 300W Xe lamp) With a cutoff filter (λ＞420 nm)	480min 6 cycles	[91]

SnO_2/g-C_3N_4	50ml 0.01mmol/L MB	5mg	85% in 100min	g-C_3N_4:35% in 100min SnO_2:26% in 100min	-	AM 1.5G simulated sunlight (100mw/cm^2)	800min 8 cycles	[44]
Flower like SnO_2/g-C_3N_4	40ml 10mg L^{-1} RhB	40mg	-	-	0.0289mi n^{-1}	300W high pressure Xe lamp(λ=290-800 nm)	480min 4 cycles	[38]
Ag/SnO_2/g-C_3N_4	40ml 20mg L^{-1} 2,4-DCP	0.2g	-	g-CN	8	150W Xe lamp with a 420nm cutoff filter	-	[87]
	CO_2	0.1g		g-CN	10	-	-	
SnO_2/S-g-C_3N_4	100ml 8mg L^{-1} MB	0.1g	94.8% in 150min	-	-	300W Hg lamp (λ＞400 nm)	-	[65]
SnO_2/g-C_3N_4	50ml 5mg L^{-1} RhB	1g L^{-1}	≈99% in 10min	-	-	10W LEDs (λ=416 nm)	-	[47]
SnO_2/g-C_3N_4	50ml 5.5mg L^{-1} MB	28mg	41.2±4.1% in 3h	g-C_3N_4:40.8±11% in 3h SnO_2:4.9±1.4% in 3h	-	400W Hg vapor lamp with a 400 nm cutoff filter	-	[45]

$Sb/SnO_2/g\text{-}C_3N_4$	5ml of solution (MeCN/TEOA=4:1) CO_2	30mg	CO:4.49 μmol $g^{-1}h^{-1}$ CH_4:0.60 μmol $g^{-1}h^{-1}$	BCN:CO:0.21 μmol $g^{-1}h^{-1}$; CH_4:0 μmol $g^{-1}h^{-1}$ PCNNS:CO:0.93 μmol $g^{-1}h^{-1}$; CH_4:0.11 μmol $g^{-1}h^{-1}$ SSOP:CO:0.35 μmol $g^{-1}h^{-1}$; CH_4:0.16 μmol $g^{-1}h^{-1}$	-	300W Xe lamp (λ＞420 nm)	15h 3 cycles	[62]
	IPA	-	Acetone:565.61 ppm h^{-1}	BCN:Acetone:62.03 ppm h^{-1} PCNNS:Acetone:276.77 ppm h^{-1} SSOP:Acetone:11.4 ppm h^{-1}	-			
SnO_2 QDs /g-C_3N_4	600 ppb NO	400mg	32% in 30min	g-C_3N_4:19% in 30min (with a large number of NO2 toxic byproducts) SnO_2:17% in 30min	1.7 1.9	150W tungsten halogen lamp (λ＞420 nm)	90min 3 cycles	[113]
SnO_2 QDs /g-C_3N_4			94% in 180min	SnO_2:21% in 180min g-C_3N_4:45% in 180min		-	5 cycles	[54]
	100ml 10ppm MO	100mg	73% in 180min	g-C_3N_4:15% in 180min g-C_3N_4/SnO_2 PM:20% in 180min		300W Xe lamp (λ＞420 nm)	520min 3 cycles	
SnO_2/g-C_3N_4	45ml deionized water with 5ml triethanolamine (with Pt)	50mg	H_2:900 μmol $g^{-1}h^{-1}$	g-C_3N_4(with Pt): H_2:650 μmol $g^{-1}h^{-1}$		300W Xe lamp (λ＞400 nm)	-	[29]
g-C_3N_4/SiO_2/SnO_2	100ml 0.01g/L RhB	5mg	95.10% in 90min	SiO_2/SnO_2: 21.65% in 90min g-C_3N_4 and SiO_2/SnO_2 PM: 76.19% in 90min	-	500W Xe lamp	900min 10 cycles	[42]

	100ml 0.01g/L MB		99.73% in 50min	SiO_2/SnO_2:21.53% in 90min			500min 10 cycles	
	100ml 0.01g/L MO		95.58% in 50min	SiO_2/SnO_2:16.31% in 90min			500min 10 cycles	
SnO_2/ B-P-g-C_3N_4	Water(3 ml)/NaOH CO_2	0.2g	49 μmol g^{-1} 8h	CN: CH_4:5.7 μmol g^{-1} 8h P-CN: CH_4:18 μmol g^{-1} 8h B-P-CN: CH_4:37 μmol g^{-1} 8h		300W Xe lamp (λ＞420 nm)	-	[66]
	810ppm acetalaehyde (with 20% O_2 and 80% N_2)	0.1g	-	-	7 times than CN	150W Xe lamp (λ＞420 nm)	-	
	80ml 10mg L^{-1} phenol		-	-			-	
SnO_2/g-C_3N_4	20ml 10mg L^{-1} MB	3.5g	99.38% in 75min	SnO_2:85% in 75min g-C_3N_4:19% in 90min Photolysis: 6.8% in 90min	-	A light setup (400W,λ＞500 nm)	375min 5 cycles	[34]
	20ml 10mg L^{-1} CR	-	96.01% in 90min	SnO_2:95.41% in 90min	-		-	
g-C_3N_4-SnO_2/TiO_2/Ti	5ml MiliQ water with 5.0 vol% acetic acid	-	CO2:	-	-	400W high-pressure mercury lamp	3 cycles	[93]

	5ml MiliQ water with 5 vol% 2-propanol	-	Acetone：0.055676μmol h^{-1}	SnO_2/TiO_2/Ti Acetone：0.001971μmol h^{-1} g-C_3N_4/TiO_2/Ti Acetone：0.018255μmol h^{-1}	-	300W xenon lamp(λ＞420 nm)		
	7ml of E. coli suspension in sterile 0.9% saline solution	-	-	-	-	A Xe lamp with UV-35(λ＞350 nm)		
SnO_2 QDs/ g-C_3N_4	100ml 50 mg L^{-1} RhB	100g 150g	90% in 100min 90% in 60min	SnO_2 -	250 times -	Visible light	3 cycles	[35]
SnO_{2-x}/g-C_3N_4	100ml 10 mg L^{-1} RhB	0.1g	＞90% in 80min	-	-	A spherical Xe lamp(800 nm ＞λ＞420 nm)	10 cycles	[39]
	100ml 50 mg L^{-1} phenol	0.1g	40% in 90min	-			-	
	CO_2	20mg	22.7μmol h^{-1} g_{cat}^{-1}	g-C_3N_4 ： 5.32μmol h^{-1} g^{-1}			-	